The Astrophysical Journal, 856:102 (23pp), 2018 April 1 https://doi.org/10.3847/1538-4357/aab03e

Hubble Space Telescope Observations of Extended [O III]λ5007 Emission in Nearby QSO2s: New Constraints on AGN Host Galaxy Interaction

Travis C. Fischer[1,17], S. B. Kraemer[2], H. R. Schmitt[3], L. F. Longo Micchi[2], D. M. Crenshaw[4], M. Revalski[4,18], M. Vestergaard[5,6], M. Elvis[7], C. M. Gaskell[8], F. Hamann[9], L. C. Ho[10], J. Hutchings[11], R. Mushotzky[12], H. Netzer[13], T. Storchi-Bergmann[14], A. Straughn[1], T. J. Turner[15], and M. J. Ward[16]

[1] Astrophysics Science Division, Goddard Space Flight Center, Code 665, Greenbelt, MD 20771, USA; travis.c.fischer@nasa.gov
[2] Institute for Astrophysics and Computational Sciences, Department of Physics, The Catholic University of America, Washington, DC 20064, USA
[3] Naval Research Laboratory, Washington, DC 20375, USA
[4] Department of Physics and Astronomy, Georgia State University, Astronomy Offices, 25 Park Place, Suite 600, Atlanta, GA 30303, USA
[5] Dark Cosmology Centre, Niels Bohr Institute, University of Copenhagen, Juliane Maries Vej 30, DK-2100 Copenhagen Ø, Denmark
[6] Steward Observatory and Department of Astronomy, University of Arizona, 933 N. Cherry Avenue, Tucson AZ 85721, USA
[7] Harvard-Smithsonian Center for Astrophysics, 60 Garden Street, Cambridge, MA 02138, USA
[8] Department of Astronomy and Astrophysics, University of California, Santa Cruz, CA 95064, USA
[9] Department of Physics and Astronomy, University of California, Riverside, CA 92507, USA
[10] Kavli Institute for Astronomy and Astrophysics, Peking University; School of Physics, Department of Astronomy, Peking University, Beijing 100871, People's Republic of China
[11] Dominion Astrophysical Observatory, NRC Herzberg Institute of Astrophysics, 5071 West Saanich Road, Victoria, BC, V9E 2E7, Canada
[12] Department of Astronomy, University of Maryland, College Park, MD 20742, USA
[13] School of Physics and Astronomy, Tel Aviv University, Tel Aviv 69978, Israel
[14] Departamento de Astronomia, Universidade Federal do Rio Grande do Sul, IF, CP 15051, 91501-970 Porto Alegre, RS, Brazil
[15] Department of Physics, University of Maryland Baltimore County, 1000 Hilltop Circle, Baltimore, MD 21250, USA
[16] Centre for Extragalactic Astronomy, Department of Physics, University of Durham, South Road, Durham DH1 3LE, UK
Received 2017 November 3; revised 2018 February 1; accepted 2018 February 14; published 2018 March 28

Abstract

We present a *Hubble Space Telescope* survey of extended [O III] λ5007 emission for a sample of 12 nearby ($z < 0.12$), luminous Type 2 quasars (QSO2s), which we use to measure the extent and kinematics of their AGN-ionized gas. We find that the size of the observed [O III] regions scale with luminosity in comparison to nearby, less luminous Seyfert galaxies and radially outflowing kinematics to exist in all targets. We report an average maximum outflow radius of ∼600 pc, with gas continuing to be kinematically influenced by the central active galactic nucleus (AGN) out to an average radius of ∼1130 pc. These findings question the effectiveness of AGNs being capable of clearing material from their host bulge in the nearby universe and suggest that disruption of gas by AGN activity may prevent star formation without requiring evacuation. Additionally, we find a dichotomy in our targets when comparing [O III] radial extent and nuclear FWHM, where QSO2s with compact [O III] morphologies typically possess broader nuclear emission lines.

Key words: galaxies: active – galaxies: kinematics and dynamics – quasars: emission lines

1. Introduction

Active galactic nuclei (AGNs) are powered by the accretion of matter onto a supermassive black hole (SMBH), which generates massive amounts of radiation within a very small volume. Mass outflows of ionized gas, a spatially resolved component of AGN feedback, are also generated and have been thought to be critical in the chemical enrichment of the intergalactic medium (Khalatyan et al. 2008) and the self-regulation of SMBH growth (Hopkins et al. 2005). The relationship between the SMBH mass and the stellar velocity of its galaxy bulge, that is, the M_{BH}–σ relation (Kormendy & Ho 2013 and references therein), is credited to ignition of the AGN quenching star formation and evacuating gas from the bulge.

AGN feedback exists in two forms: radio jets and "AGN winds." Jets are powerful and clearly impact their host galaxies and extragalactic environments. However, they are highly focused, and strong jets occur in only 5%–10% of the AGN population (Rafter et al. 2009). Alternatively, winds are prevalent in most AGNs (Mullaney et al. 2013; Genzel et al. 2014; Woo et al. 2016), including nearby, moderate-luminosity Seyfert galaxies. AGN winds are often observed as UV and X-ray absorption lines blueshifted with respect to their host galaxies, traveling at velocities up to ∼2500 km s^{-1} within tens of parsecs from the central SMBH (Crenshaw et al. 2003; Veilleux et al. 2005; Crenshaw & Kraemer 2012; King & Pounds 2015), or emission-line gas in AGN narrow-line regions (NLRs) on larger scales (100–1000 s of pc), with outflow velocities up to ∼2000 km s^{-1} (Crenshaw & Kraemer 2005; Crenshaw et al. 2010; Müller-Sánchez et al. 2011; Fischer et al. 2013, 2014; Bae & Woo 2016; Nevin et al. 2016). This is likely to be the region where interaction between AGN and nuclear star formation occurs. One aspect not addressed in this work is molecular gas outflows. Recent studies (Veilleux et al. 2013; Cicone et al. 2014) have found evidence for molecular outflows in AGNs on large (>1 kpc) scales; however, most of the AGNs in these works are in merged systems, whereas only one source, 2MASX-J0802593+2552551, shows evidence for an ongoing merger in our sample. Therefore, although we cannot rule out the presence of large-scale molecular outflows, the distribution of gas and dynamics in these AGNs are likely much different than in merged systems and more consistent with typical low-z Seyfert galaxies (Fischer et al. 2013).

[17] *James Webb Space Telescope* NASA Postdoctoral Program Fellow.
[18] National Science Foundation Graduate Research Fellow.

Recently, we used the Gemini Near-Infrared Integral Field Spectrograph (NIFS) to observe the NLR of the luminous, nearby Seyfert 2 galaxy Mrk 573 (Fischer et al. 2017). From this work, we found the NLR morphology to be consistent with an intersection between spiral arms in the host disk and ionizing radiation from the central engine, as dust lanes rotating in the host disk (also traced by molecular hydrogen emission) were found to connect to arcs of ionized gas inside the AGN ionizing bicone from outside the field of ionizing radiation. Host disk gas inside the ionizing field at small radii ($r <$ 750 pc) is radiatively driven away from the central engine and forms the NLR of the AGN, while ionized gas at greater radii follows the rotation kinematics of the host disk as part of the extended NLR (ENLR; Unger et al. 1987). Applying these findings to other, similar high-resolution kinematics studies of nearby, inclined Seyferts (Das et al. 2005, 2006; Crenshaw et al. 2010; Storchi-Bergmann et al. 2010; Müller-Sánchez et al. 2011; Fischer et al. 2013), where projection effects on outflow distances are small, we find that gas in the radially driven NLRs (i.e., gas with predominantly radial velocity structure) typically extend less than 1 kpc from the central engine. These observations question how successful AGN feedback is on the galaxy-bulge scales that may be required in a bulge-quenching, negative-feedback scenario. One aspect that may explain these findings is that Seyferts are relatively low-luminosity AGNs. Therefore, outflows may not be powerful enough in these nearby AGNs to drive gas out to bulge-radius distances.

While one would expect that the power of these outflows would scale with luminosity, as suggested by Ganguly & Brotherton (2008), ground-based studies of Type 2 quasars (QSO2s; Greene et al. 2011; Liu et al. 2013b; Harrison et al. 2014; McElroy et al. 2015) have found mostly chaotic, low-velocity [O III] profiles attributed to AGN activity, with kiloparsec-scale, high-velocity outflows being exceptionally rare. Studies of SDSS J135646.11+102609.1 (Greene et al. 2011, 2012), for example, find outflows on scales of ~10 kpc, with deprojected velocities of $\sim$1000 km s^{-1}. Additionally, previous analysis of optical long-slit observations of the nearby QSO2 Mrk 34 (Fischer et al. 2013) measured bright, nonrotational kinematics (i.e., outflows) at distances of >1 kpc. However, the absence of evidence for such outflows in a majority of observations raises the question of whether kiloparsec-scale winds exist in most QSO2s. If they do not, it follows that outflows are not a critical component of quasar-mode feedback and the evolution of galaxy bulges, implying that the star formation is quenched in bulges by other means. As such, we have obtained Hubble Space Telescope (*HST*) imaging and spectroscopy of 12 of the most luminous QSO2s within $z = 0.12$, through Hubble Program ID 13728 (PI: Kraemer) and archive observations of Mrk 34, to map [O III] velocities and widths as a function of radial distance and determine the extent of AGN-driven outflows in each system.

2. Sample, Observations, and Measurements

2.1. Target Selection

Our sample is listed in Table 1 and includes 12 of the 15 most luminous targets from the Reyes et al. (2008) QSO2 sample under $z = 0.12$. Our choice of distance limit was made to ensure our ability to map the structure of the [O III] gas at scales of several 100 pcs for our most distant targets, while opting for the most luminous targets ensures that we are studying AGNs more luminous than the Seyfert galaxies in our previous kinematic studies. All targets have a log $L_{[\mathrm{O\,III}]} \geqslant$ 42.28, satisfying the conventional *B*-band absolute-magnitude criterion of a "quasar," $M_B < -23$, where a corresponding $L_{[\mathrm{O\,III}]}$ is $>3 \times 10^8 L_\odot$ (Zakamska et al. 2003), and are among the top 25% of QSO2s under $z = 0.3$ in the Reyes et al. (2008) sample. The majority of the sample are radio quiet, with a few being intermediately radio loud, which indicates, in analogy to nearby Seyferts, that outflows are not likely to be jet driven. Minimum SMBH mass estimates required to produce the observed [O III] radiation range between $10^{7.7}$ and $10^{8.3}$ $M_\odot$, calculated using the [O III] measurements from Reyes et al. (2008) and assuming an AGN radiating at Eddington with $L_{\mathrm{bol}} = L_{[\mathrm{O\,III}]} \times 3500$ (Heckman et al. 2004). If these sources are heavily reddened, the bolometric correction and resulting black hole masses would be larger. In order to best sample extended NLR kinematics in each target, Type 2 QSOs were chosen rather than QSO1s, as AGN-ionized gas morphologies in QSO1s can be strongly foreshortened by projection effects.

2.2. HST Observations

Knowledge of the ionized-gas morphology of each AGN was required in order to properly place the Space Telescope Imaging Spectrograph (STIS) long slit across its greatest extension in each AGN. Therefore, the observing program for our sample was performed in a two-step process: obtain narrow-band images of each AGN to determine ideal STIS position angles, and return at a later date for the follow-up spectroscopic observation. Images were obtained for each QSO2 in our sample using FR505N and FR551N filters, chosen depending on the redshift of each target to observe [O III], with the Wide-Field Channel (WFC) of *HST*/ACS. Continuum observations were obtained using the FR647M filter, selected to provide a relatively broad continuum region free of strong emission lines, for continuum subtraction. Images were obtained between 2014 October 29 and 2015 July 8.

Long-slit spectra were obtained using *HST*/STIS, with the CCD detector employing the $52'' \times 0.''2$ slit. Spectra were obtained between 2015 January 29 and 2016 March 3, using either the G430M or G750M medium-dispersion grating, also dependent on the redshift of each target, to observe [O III]. Spectral resolutions for the G430M and G750M gratings are 0.56 and 1.1 Å (for bandwidths of 286 and 572 Å), respectively, with an angular resolution of $0.''051$ per pixel in the cross-dispersion direction. Slit position angles for each observation were aligned within 5° of the projected axis of the ionized gas observed in the previously obtained *HST* imaging. Spectra were taken as a combination of three exposures of similar exposure lengths optimized to maximize available observing time in a single orbit. Observations were dithered by $\pm 0.''25$ along the slit with respect to the first spectrum to avoid problems due to hot pixels, and wavelength calibration lamp spectra were taken during Earth occultation.

Our sample also includes archival imaging and spectroscopic observations (Proposal IDs 10873 and 8253, respectively) of the QSO2 Mrk 34, as it matches the criteria of our sample and has similar *HST* imaging (WFPC2 for Mrk 34 versus ACS for the rest of the sample) and long-slit observations. Archival Mrk 34 observations were gathered from the Mikulski Archive for Space Telescopes (MAST). [O III] imaging for this target

Table 1
QSO2 Sample Characteristics and *HST* Observations Summary

Target	R.A. (2000)	Decl. (2000)	Redshift	Scale (kpc/″)	log $L_{[O\ III]}$ erg s^{-1}	Min. M_{BH} log($M/M_{\odot}$)	$S_{20\ cm}$ (mJy)	Filter/ Grating	Total Exp (s)	Center λ (Å)	PA_{slit} (°)
2MASX J07594101 +5050245	07 59 40.9	+50 50 23	0.054	1.02	42.35	7.8	45.55	FR647M	200	5803.1	···
								FR551N	1956	5280.5	···
								G430M	2270	5216.0	102.7
2MASX J08025293 +2552551	08 02 52.9	+25 52 55	0.081	1.48	42.35	7.8	29.37	FR647M	200	5949.6	···
								FR551N	1788	5413.7	···
								G430M	1997	5471.0	−156.4
MRK 34	10 34 08.6	+60 01 52	0.051	0.95	42.39	7.8	17.01	F467M	5200	4670.0	···
								F547M	7700	5483.0	···
								G430M	1500	5216.0	152.6
2MASX J11001238 +0846157	11 00 12.4	+08 46 15	0.101	1.80	42.69	8.1	58.54	FR647M	200	6056.1	···
								FR551N	1769	5510.1	···
								G430M	1883	5471.0	160.6
SDSS J115245.66 +101623.8	11 52 45.7	+10 16 23	0.070	1.30	42.28	7.7	3.56	FR647M	200	5887.8	···
								FR551N	1773	5358.0	···
								G430M	1944	5471.0	−169.9
FIRST J120041.4 +314745	12 00 41.4	+31 47 46	0.116	2.04	42.89	8.3	7.31	FR647M	200	6138.5	···
								FR551N	1804	5585.6	···
								G750M	2015	5734.0	−89.7
2MASX J13003807 +5454367	13 00 38.1	+54 54 36	0.088	1.59	42.47	7.9	2.19	FR647M	200	5989.4	···
								FR551N	1956	5449.4	···
								G430M	2210	5471.0	164.4
2MASX J14054117 +4026326	14 05 41.2	+40 26 32	0.081	1.47	42.29	7.7	16.81	FR647M	200	5946.6	···
								FR551N	1863	5411.7	···
								G430M	2177	5471.0	137.1
B2 1435+30	14 37 37.9	+30 11 01	0.092	1.66	42.38	7.8	63.91	FR647M	200	6010.4	···
								FR551N	1804	5469.3	···
								G430M	2055	5471.0	80.1
MRK 477	14 40 38.1	+53 30 16	0.038	0.72	42.30	7.7	57.59	FR647M	200	5707.5	···
								FR505N	1912	5191.5	···
								G430M	2224	5216.0	29.8
2MASX J16531506 +2349431	16 53 15.1	+23 49 42	0.103	1.83	42.54	8.0	6.93	FR647M	200	6072.0	···
								FR551N	1779	5525.0	···
								G430M	2169	5471.0	−104.9
2MASX J17135038 +5729546	17 13 50.3	+57 29 54	0.113	1.97	42.53	8.0	7.62	FR647M	200	6122.7	···
								FR551N	2017	5571.7	···
								G750M	2214	5734.0	27.8

Note. Columns 1–4 list each target and their coordinates and redshift. Column 5 lists the cosmology-corrected scale from the NASA Extragalactic Database. Column 6 lists the [O III] luminosity from Reyes et al. (2008). Column 7 lists the minimum SMBH mass required to produce the observed radiation, assuming an AGN radiating at Eddington with $L_{bol} = L_{[O\ III]} \times 3500$ (Heckman et al. 2004). Column 8 lists radio fluxes from Reyes et al. (2008). Columns 9 and 10 list the filter/grating and exposure time of each data set. Column 11 lists central wavelengths for each observation. Column 12 lists spectroscopic long-slit position angles.

is produced from F547M WFPC2 imaging with F467M continuum subtraction, as alignment between [O III] and continuum imaging is required to properly map the STIS slit locations to the [O III] imaging. Further details of all *HST* observations for our entire sample are listed in Table 1.

2.3. Data Reduction

Data reduction for continuum and on-band images followed the standard *HST* pipeline procedures. On-band and continuum images were observed sequentially, not requiring realignment between images. The flux calibration of the FR647M and F467M continuum images and the FR505N, FR551N, and F547M on-band images was done in the standard way, using the information available on the image headers. Photometrically calibrated, 2D-rectified images of each long-slit observation were processed using Interactive Data Language software, where multiple dithered observations of each target were aligned and combined into a single averaged data set. Extracted, spatially resolved [O III]$\lambda\lambda$4959, 5007 emission lines from each combined data set are shown in Figure 1.

The final [O III] images of the galaxies are presented in Figures 3–9. The lowest contour value of these images corresponds

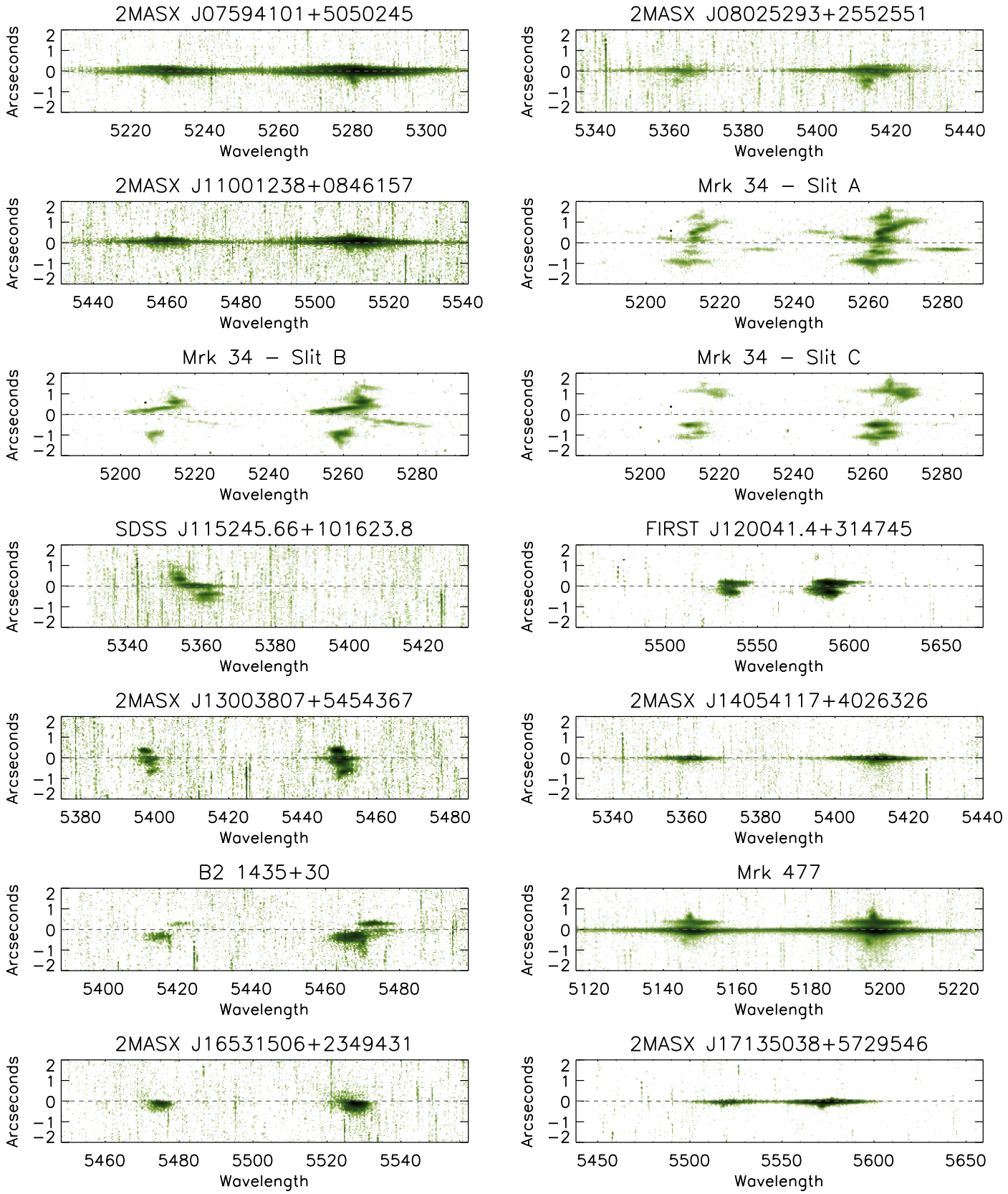

Figure 1. STIS G430M and G750M long-slit spectral images of the [O III] $\lambda\lambda$4959, 5007 lines of our QSO2 sample. Each row of a spectral image represents a 0.″05 step along the STIS long slit, with the top of each 2D spectral image corresponding to the end of the long slit at the position angle of the observations, as listed in Table 1. Images are displayed with a minimum flux level of 3×10^{-17} erg cm^{-2} s^{-1} Å^{-1}. Observations for SDSS J115245.66+101623.8 do not contain [O III] λ4959 line emission as the line is outside the observed G430M wave-band coverage.

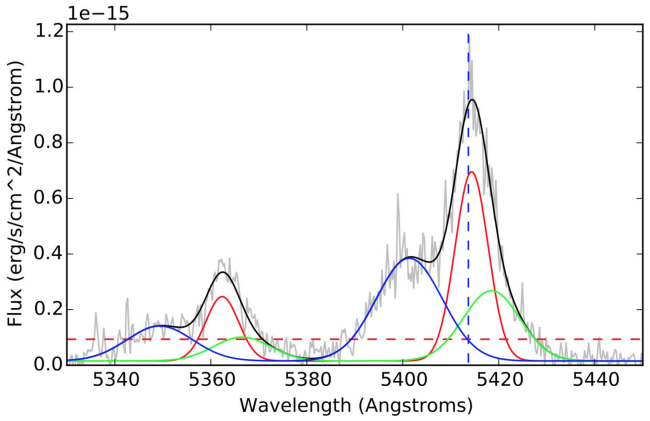

Figure 2. [O III] λλ4959, 5007 emission-line component fitting example over the continuum peak (0.″0 offset) in 2MASX J08025293+2552551. Gaussian fits to [O III] λ4959 used centroid and width parameters fixed to be identical to those of [O III] λ5007, with height fixed to be one-third of the [O III] λ5007 Gaussian. The gray line represents STIS spectral data. The solid black line represents the total model. Blue, green, and red lines represent individual Gaussian components with first-, second-, and third-widest FWHM measurements, respectively. The vertical dashed blue line represents the [O III] λ5007 wavelength at systemic velocity. The horizontal dashed red line represents the 3σ continuum-flux lower limit for the [O III] λ5007 Gaussian height in our fitting.

to the 3σ level above the background in surface brightness, with interior contours increasing in powers of 2 × 3σ.

2.4. [O III] Spectroscopic Fitting

[O III] λ5007 kinematics and fluxes in our STIS observations were measured by fitting the emission line in each row of the 2D STIS CCD spectral image with Gaussians in an automated routine (Figure 2). Our fitting process, previously discussed in depth in Fischer et al. (2017), uses the Importance Nested Sampling algorithm as implemented in the MultiNest library (Feroz & Hobson 2008; Feroz et al. 2009, 2013; Buchner et al. 2014) to compute the logarithm of the evidence, *lnZ*, for models containing a continuum plus zero, one, two, and three Gaussian components per emission line. When comparing two models, such as a model with zero Gaussians (M_0) and a model with one Gaussian (M_1), the simpler model is chosen unless the more complex model, M_1, has a significantly better evidence value, $|\ln(Z_1/Z_0)| > 5$ (99% more likely). Models for measuring [O III] λ5007 simultaneously fit a second set of components to [O III] λ4959 in order to properly account for flux contributions from wing emission between both lines. Gaussian centroid and width parameters of the [O III] λ4959 line were fixed to be identical to the parameters used in fitting the [O III] λ5007 line, and the flux was fixed to be one-third that of the [O III] λ5007 flux parameter. Models for SDSS J115245.66+101623.8 did not fit the [O III] λ4959 line as the redshift of this target placed the line outside the observed G430M wave-band coverage.

Initial input parameters in our models are selected based on physical considerations. The centroid position for each Gaussian was limited to a 40 Å range around the systemic [O III] wavelength that contained the entirety of the line profile throughout each long-slit data set. The Gaussian standard deviation ranged from the spectral resolution of the G430M/G750M gratings to an artificial limit of 15 Å ([O III] FWHM ∼ 2000 km s^{-1}). The Gaussian height was permitted to range from a minimum height of 3 times the standard deviation of the adjacent continuum (3σ) to a virtually unbound maximum height restriction of 3σ × 10^8.

2.5. Host Disk Elliptical Fitting

As illustrated in Fischer et al. (2017), spatially resolved, AGN-ionized gas can be explained as illuminated material located near the plane of the host disk, where rotating molecular gas outside the AGN area of influence in Mrk 573 connects to the ionized-gas structures inside the AGN area of influence. Therefore, if we assume that a majority of AGN ionized-gas structure in other Type 2 AGNs also resides in their host disks, we can employ information on the host disk orientation of each target to deproject *HST* measurements for our QSO2 sample and determine true physical distances. Continuum imaging of our sample was obtained in our *HST* data set, but these observations were intended for continuum subtraction of [O III] imaging and are too shallow for independent orientation analysis. Measurements of host disk ellipticities (*e*) and major axis position angles (PA_{MA}) were therefore obtained by fitting ellipses to isophotes in *gri* Sloan Digital Sky Survey (SDSS; York et al. 2000; Eisenstein et al. 2011) imaging of each galaxy using the `ellipse` routine in the STSDAS package of IRAF. Ellipses were fit from the inner ∼0.″2 of each image out to where flux levels reached a 3σ level above the background in all bands. The background level and its standard deviation were determined from blank regions within the SDSS CCD field of each galaxy. Targets with interacting morphologies, 2MASX J08025293+2552551, B2 1435+30, and Mrk 477, were fit to a 5σ level, and FIRST J120041.4+314745, which is immediately adjacent to a neighboring galaxy, was fit to a 9σ level to avoid fit disturbances in low-flux isophotes. Ellipse parameters obtained from the fit of each SDSS image are shown in Appendix Figures 13–18. Final values of PA_{MA} and *e* used for our calculations, as listed in Table 2, are the average of values taken from each band at the greatest distance where the minimum signal-to-noise ratio (S/N) measurements exist in all bands. The difference in host major axis and STIS observation position angles is also provided in Table 2 as PA_{diff}.

3. Results

3.1. Morphologies

Continuum-subtracted [O III] images were used to measure the projected extension of AGN ionization in these galaxies. Using the continuum centroid as the nucleus location in each galaxy, we measured the length between the continuum centroid and the farthest radial extent in each [O III] image (R_{max}), as determined by the 3σ surface brightness contour in each image. The R_{max} measurements are illustrated in the left side of Figures 3–6 as solid black circles. To distinguish targets that have similar [O III] extents but different flux distributions, we also provide the radius that encompasses 90% of the flux inside R_{max}, $R_{90\%}$, which is smaller for centrally peaked [O III] sources and larger for sources with bright, extended structures. Position angles (PAs) of the [O III] emission axis in each target were measured by eye. [O III] emission in three galaxies, 2MASX J11001238+0846157, 2MASX J14054117+4026326, and 2MASX J17135038 +5729546, was not extended enough to accurately determine

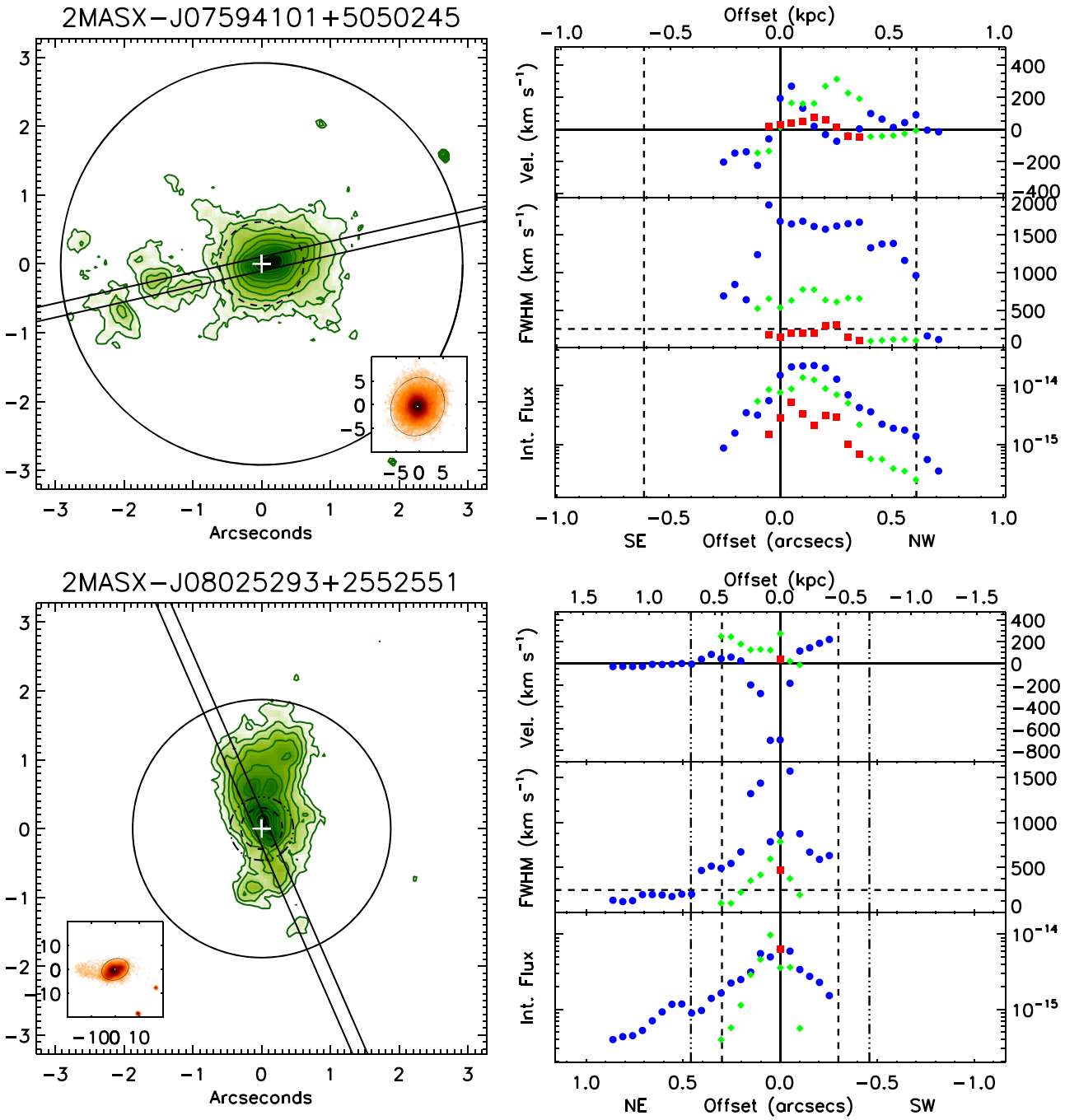

Figure 3. *HST* and SDSS data sets for 2MASX J07594101+505245 and 2MASX J08025293+2552551. Left: 5″ × 5″ continuum-subtracted [O III] λ5007 images of each target. [O III] flux contours start at 3σ over background and increase in powers of 2 times 3σ (i.e., 3σ × 2^n). The position of the nucleus, measured at the continuum-image flux peak of each target, is plotted as a white cross. Dashed, dot-dashed, and solid circles represent R_{out}, R_{dist} (when different than R_{out}), and R_{max} radii, respectively. Slits depict the position of STIS long-slit positions. Inset images display 20″ × 20″ and 40″ × 40″ *r*-band SDSS images of 2MASX J07594101 +505245 and 2MASX J08025293+2552551, respectively, with the host disk elliptical fit used in our analysis overplotted. North is up and east is left in all images. Right: velocities, FWHMs, and integrated fluxes (ergs s^{-1} cm^{-2}) for each emission-line component of our kinematic fits to the [O III] λ5007 emission line along our *HST*/STIS medium-resolution observations. Kinematic data points are marked as blue circles, green diamonds, and red squares corresponding to components with first-, second-, and third-widest FWHM measurements, respectively. The horizontal dashed line in FWHM plots signifies the approximate limit for nondisturbed kinematics of 250 km s^{-1}. Vertical dashed and dot-dashed lines represent the maximum radius of observed outflows (R_{out}) and disturbed kinematics (R_{dist}; when different than R_{out}), respectively. The R_{dist} radii for 2MASX J07594101+505245are equal in size to R_{out}. The R_{out} and R_{dist} radii in each target are mirrored across the nucleus to illustrate the maximum extent of each region and associate the kinematics to what is observed in imaging, even if no data points exist out to those radii on a given side of the nucleus.

a PA. Table 3 gives the measured values of R_{max}, $R_{90\%}$, PA, and the 3σ flux density used to trace the extent of the [O III] gas, with angular radii converted to true radii using scales listed in Table 1 derived from the luminosity distance of each target.

3.2. Kinematics

We mapped the observed ionized-gas kinematics in each galaxy by extracting Gaussian parameters from the best fit to the [O III] λλ4959, 5007 emission line for each row of the 2D spectral

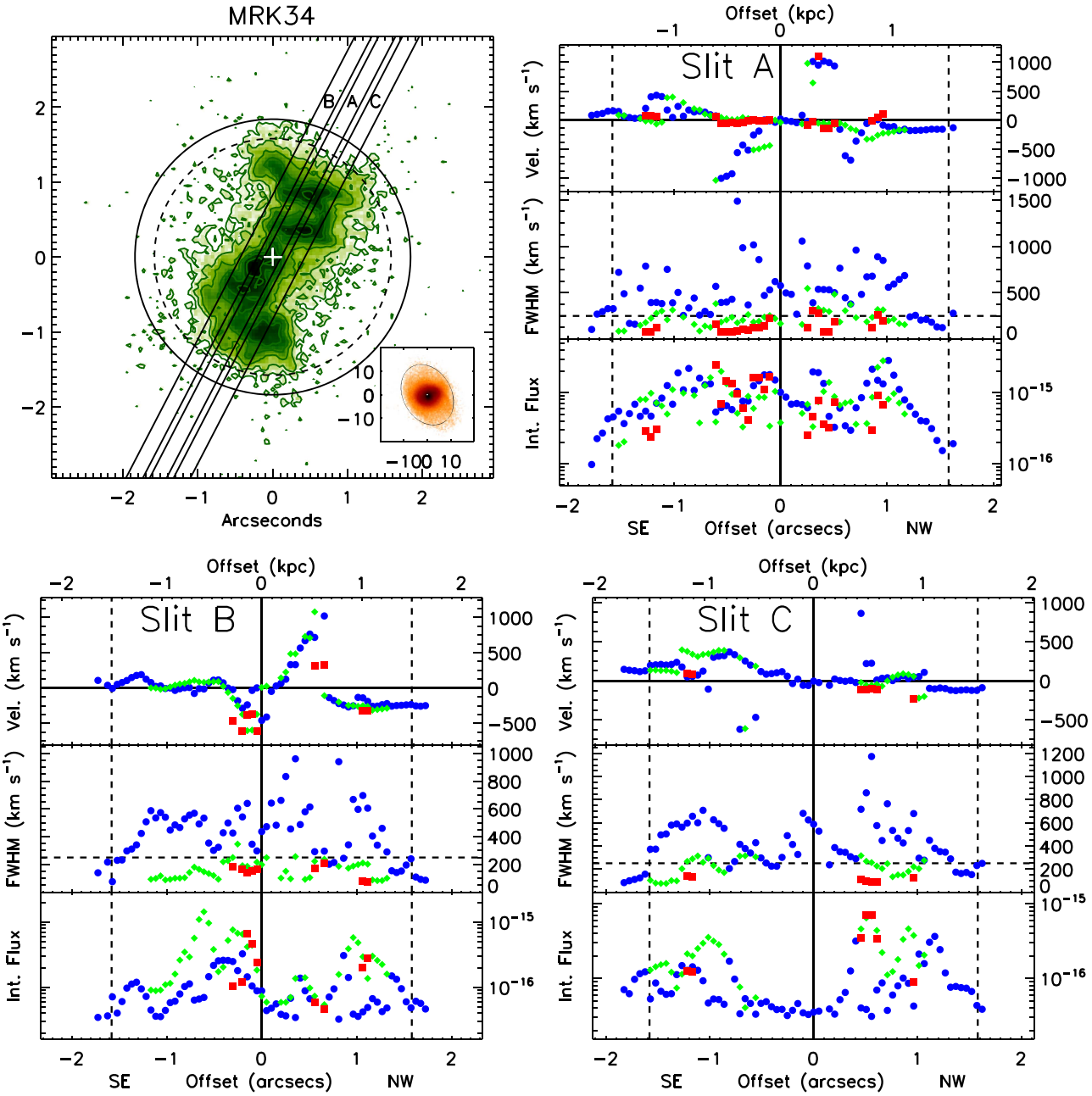

Figure 4. Same as Figure 3 for Mrk 34. Inset image: the *r*-band SDSS image is 40″ × 40″, with the host disk ellipticals fit to 3σ. The $R_{\rm dist}$ radii for Mrk 34 are equal in size to $R_{\rm out}$; $R_{\rm out}$ is measured as the maximum radius measurement across all three long-slit observations.

images of our long-slit data, as seen in Figure 1. Resultant velocities (given in the rest frame of the galaxy and using a vacuum rest wavelength of 5008.24 Å), FWHMs, and integrated fluxes (integrated under the Gaussian) for individual Gaussian components along each QSO2 long-slit spectrum in our sample are shown in the right side of Figures 3–6, with left to right progression representing 0.″05 steps along the STIS long slit and a 0.″0 offset located over the continuum centroid observed in imaging. Spectra containing multiple Gaussian components, as seen in Figure 2, are sorted by measured FWHM, with blue circles, green diamonds, and red squares corresponding to first-, second-, and third-widest FWHM components, respectively. Specifically, Gaussian parameters extracted from the emission-line fits in Figure 2 are seen reproduced at the 0.″0 offset in the kinematics plots of 2MASX J08025293+2552551 in Figure 3.

Kinematic analysis of the [O III] gas was performed based on our findings from Fischer et al. (2017), where we found the influence of the central AGN to be stratified into two regions extending from the nucleus. At small radii, outflows are visible as emission lines deviating from the overall rotation pattern of the system or emission lines that possess multiple components that travel at different velocities from one another in the NLR. At greater radii, gas is ionized by AGN radiation but possesses velocities and FWHMs consistent with gas in rotation with the host galaxy, as derived by stellar kinematics, in the extended NLR (ENLR). Applying these qualifications to the kinematics of our current sample, we can measure the extent of the outflowing gas within the observed [O III] emission of each target. In doing so, we also find that several targets exhibit a third composite set of AGN kinematics where the gas appears

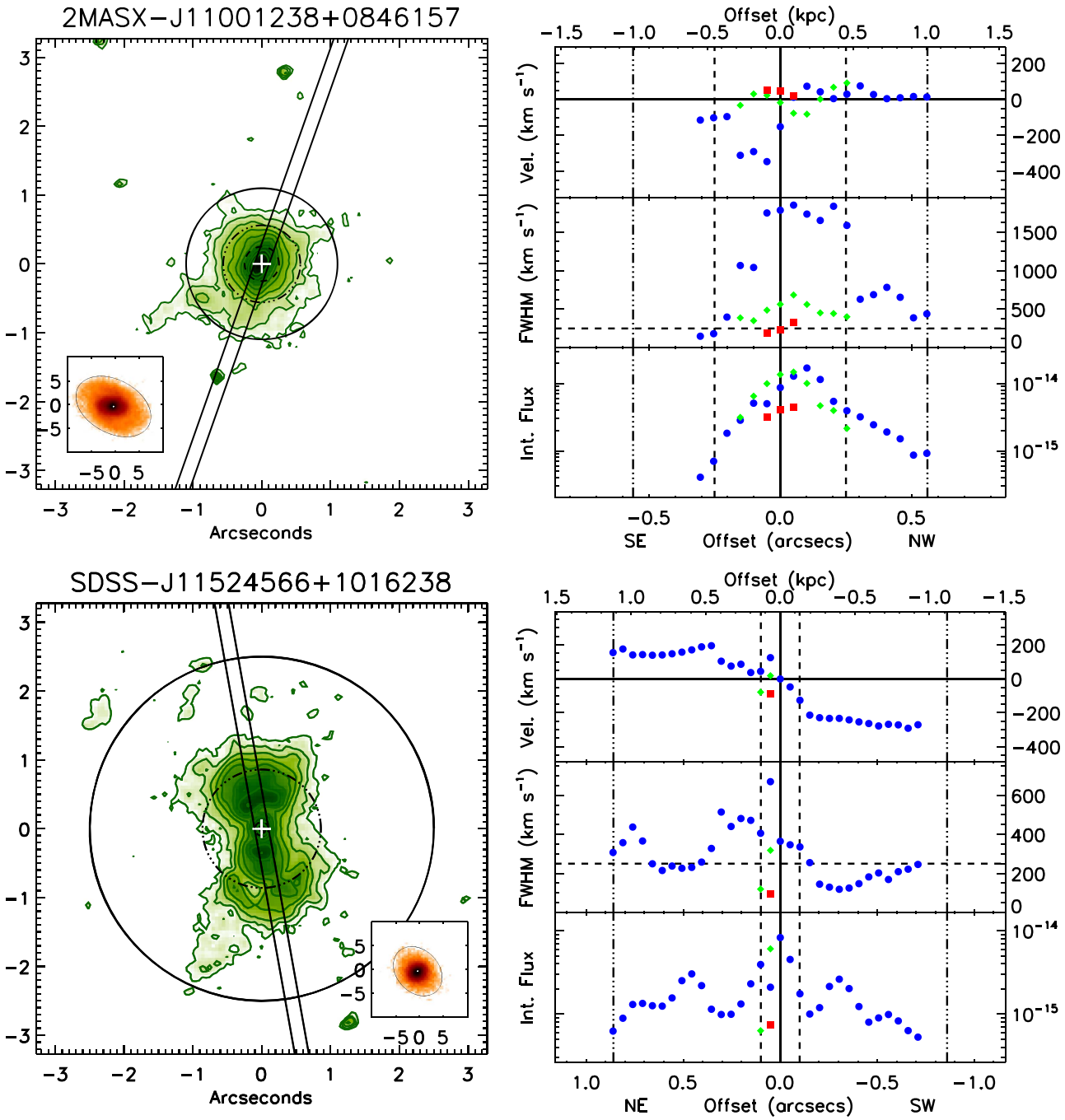

Figure 5. Same as Figure 3 for 2MASX J11001238+0846157 and SDSS J115245.66+101623.8. Inset image: the *r*-band SDSS images are 20″ × 20″, with host disk ellipticals both fit to 3σ.

to be in rotation but is experiencing some influence by the AGN as FWHM measurements are found to be consistently >250 km s^{-1}, indicative of some kinematic disturbance (Bellocchi et al. 2013; Ramos Almeida et al. 2017). While the gas sampled in these regions is not outflowing, it is being disturbed by the AGN, so we reference these regions as "disturbed" kinematics. We specifically classify the stratification of outflow, disturbed, and nondisturbed rotation kinematics below, from which we measure the extent of outflowing and AGN-disturbed gas in each system:

(1) AGN-driven outflows: emission lines that exhibit high centroid velocities (>300 km s^{-1}) from systemic or emission lines with multiple components. Velocities do not follow the velocity pattern of adjacent regions. The maximum radial extent of these kinematics is measured as $R_{\rm out}$, designated by dashed lines in both the STIS measurements and the ACS or WFPC2 imaging of Figures 3–9.

(2) Disturbed rotation: single-component emission lines with FWHMs > 250 km s^{-1} that exhibit low centroid velocities (<300 km s^{-1}) that follow the orderly rotation pattern observed in similar radial distances. The maximum radial extent of these kinematics is measured as $R_{\rm dist}$, marked with dot-dashed lines in Figures 3–9. Targets without $R_{\rm dist}$ dot-dashed lines have equal $R_{\rm out}$ and $R_{\rm dist}$ measurements.

(3) Nondisturbed rotation: emission lines that exhibit low centroid velocities (<300 km s^{-1}) with low FWHM

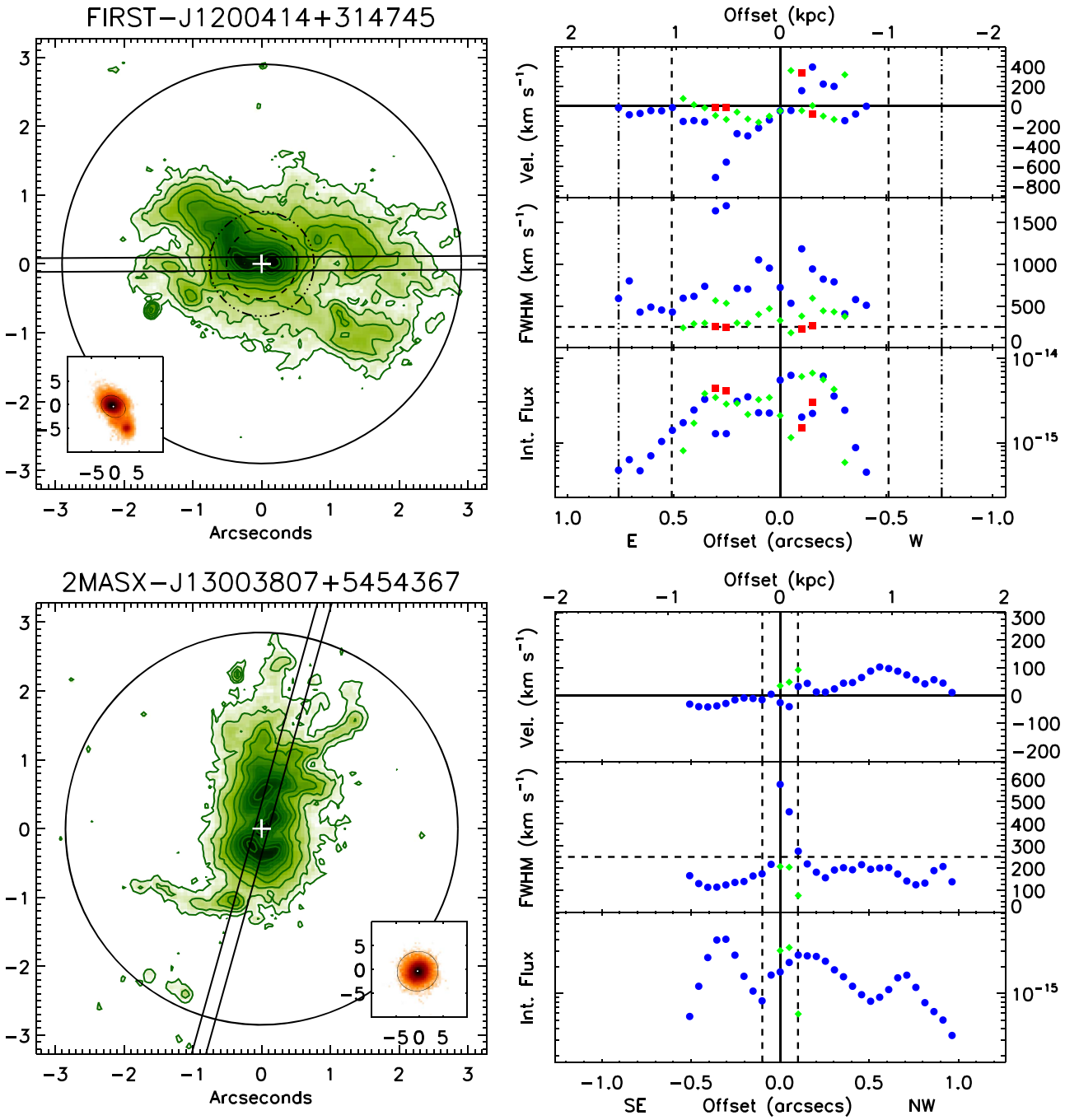

Figure 6. Same as Figure 3 for FIRST J120041.4+314745 and 2MASX J13003807+5454367. The $R_{\rm dist}$ radii for 2MASX J13003807+5454367 are equal in size to $R_{\rm out}$. Inset image: the *r*-band SDSS images are 20″ × 20″, with host disk ellipticals fit to 9σ and 3σ, respectively.

($\lesssim$250 km s^{-1}). This is consistent with rotation, where measurable nonsystemic extents exhibit blueshifts on one side of the nucleus and redshifts on the other side.

Maximum projected $R_{\rm out}$ and $R_{\rm dist}$ distances in each target are marked in the kinematics plots of Figures 3–6 and mirrored across the nucleus to illustrate the extent of each region and aid in associating the kinematics to what is observed in imaging, even if no spectroscopic data points exist out to those radii on a given side of the nucleus. Descriptions of the individual $R_{\rm out}$ and $R_{\rm dist}$ measurements for each target are provided in the Appendix, with resultant distances listed in Table 4.

We deproject our maximum distance measurements of the outflowing and disturbed gas by dividing our maximum projected distances by a scaling factor (s) calculated from the orientation of the [O III] morphology and the orientation and ellipticity of the host galaxy, as determined from our elliptical fits to the SDSS host images:

$$s = \frac{b}{\sqrt{(b\cos(\theta))^2 + \sin(\theta)^2}}, \quad (1)$$

where b is the fractional size of the minor axis relative to the major axis (i.e., $a = 1$), as determined from the ellipticity of the host ($e = 1 - \frac{b}{a}$), and θ is the difference in position angles of the host major axis and the [O III] morphology.

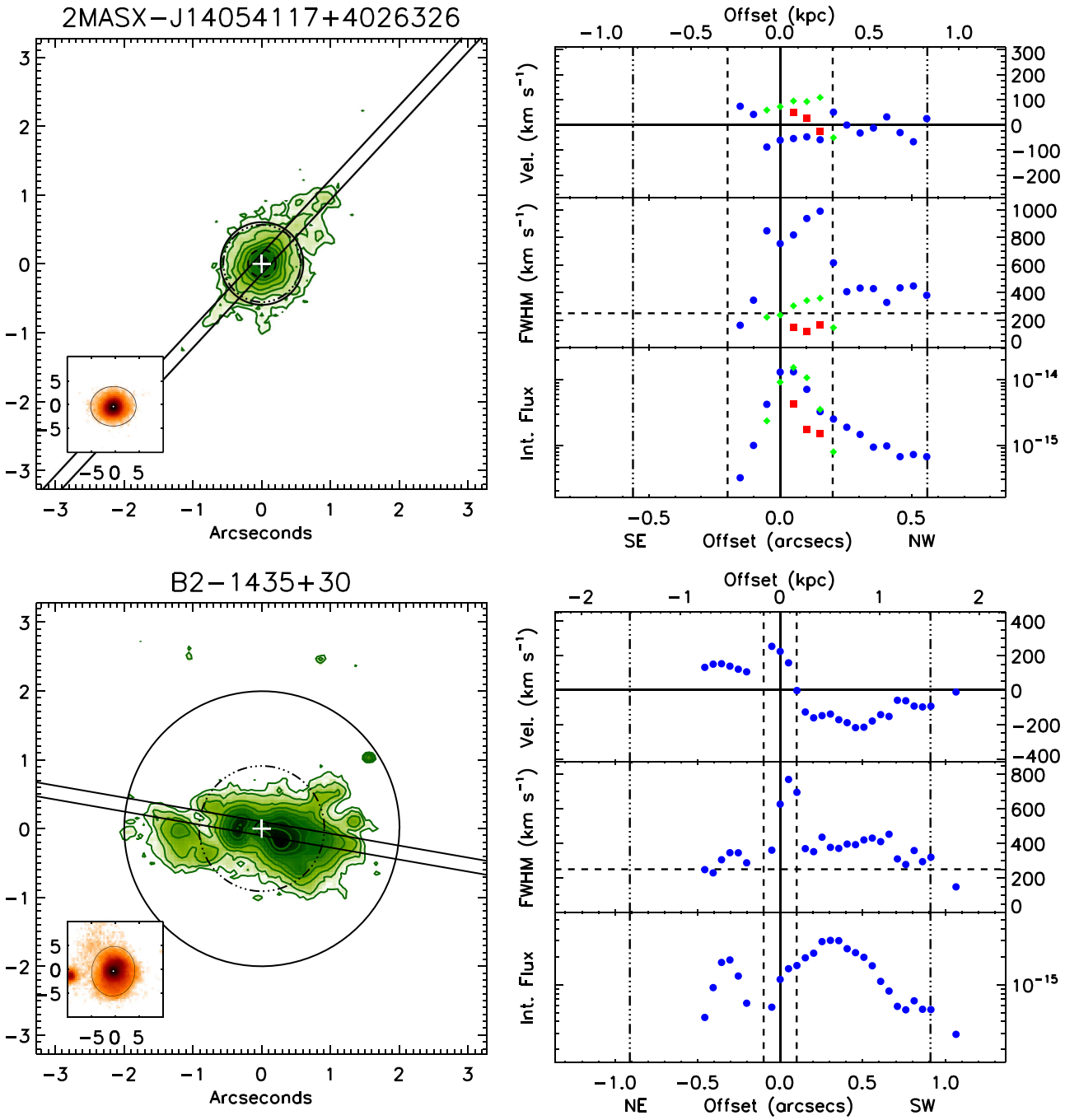

Figure 7. Same as Figure 3 for 2MASX J14054117+4026326, B2 1435+30. Inset image: the *r*-band SDSS images are 20″ × 20″, with host disk ellipticals fit to 3σ and 5σ, respectively.

Scales in targets without a clear ionized-gas position angle, 2MASX J11001238+0846157, 2MASX J14054117+4026326, and 2MASX J17135038+5729546, are the maximum deprojection of each target's measurements assuming that the difference in position angle of the host major axis and the [O III] morphology in each target is 90°. After deprojecting our initial measurements, we find that the maximum outflow radii range from 150 to 1890 pc, with a mean value of ∼625 pc, and the observed maximum disturbed radii similarly range from 160 to 1890 pc, with a mean value of ∼1130 pc. We note that measurements of disturbed gas radii extend to the full length of our observations in several targets.

4. Discussion

4.1. [O III] Extent–Luminosity Relation

Comparing our projected QSO2 [O III] extents (R_{max}), as presented in Table 3, with similar measurements (i.e., measured to similar sensitivities of $\sim 10^{-15}$ erg cm^{-2} s^{-1} arcsecond^{-1}) for nonmerging Seyfert galaxies (Schmitt et al. 2003a) and higher redshift QSO2s (Liu et al. 2013a), we find a continuous trend between [O III] extent and [O III] luminosity, as shown in Figure 10. The trend suggests higher luminosity targets produce [O III] out to greater distances. This figure contains three linear fits. The first fit (dashed line), obtained using all

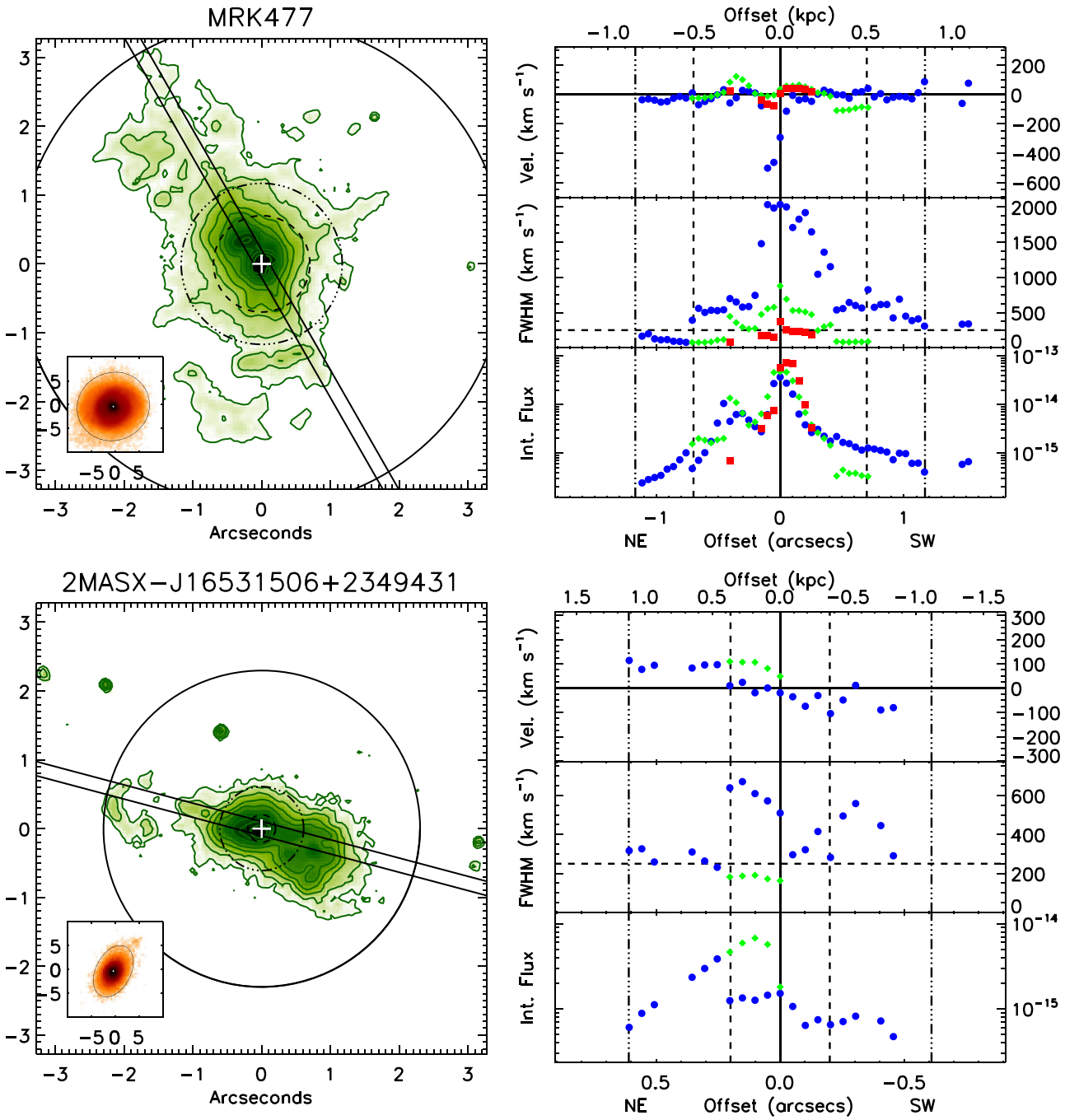

Figure 8. Same as Figure 3 for Mrk 477 and 2MASX J16531506+2349431. Inset image: the *r*-band SDSS images are $20'' \times 20''$, with host disk ellipticals fit to 5σ and 3σ, respectively.

observed galaxies, has the expression

$$\log R_{\rm max} = -18.41 + 0.52 \log L_{[\rm O\ III]}$$

with a Spearman rank of $\rho = 0.92$ and a slope uncertainty of 0.024. The second fit (solid line) was obtained only using galaxies observed with *HST*, our targets, and those from Schmitt et al. (2003b) and has the expression

$$\log R_{\rm max} = -14.85 + 0.43 \log L_{[\rm O\ III]}$$

with a Spearman rank $\rho = 0.82$ and a slope uncertainty of 0.031. The third fit (dotted line) was obtained using only *HST*-observed Seyfert 2s and QSO2s. The resulting expression is

$$\log R_{\rm max} = -14.45 + 0.42 \log L_{[\rm O\ III]}$$

with a Spearman rank $\rho = 0.88$ and a slope uncertainty of 0.031.

We find that fits from *HST*-observed targets have similar slopes of ∼0.42, with the slight offset from including Seyfert 1s likely due to projection effects. The measured slopes are steeper than the value of 0.33 found by Schmitt et al. (2003a), but shallower than the value of 0.52 observed by Bennert et al. (2002). A slope of 0.5, similar to what is found when fitting all targets, is consistent with a $1/r^2$ dilution of the ionizing radiation, assuming similar gas densities and covering factors

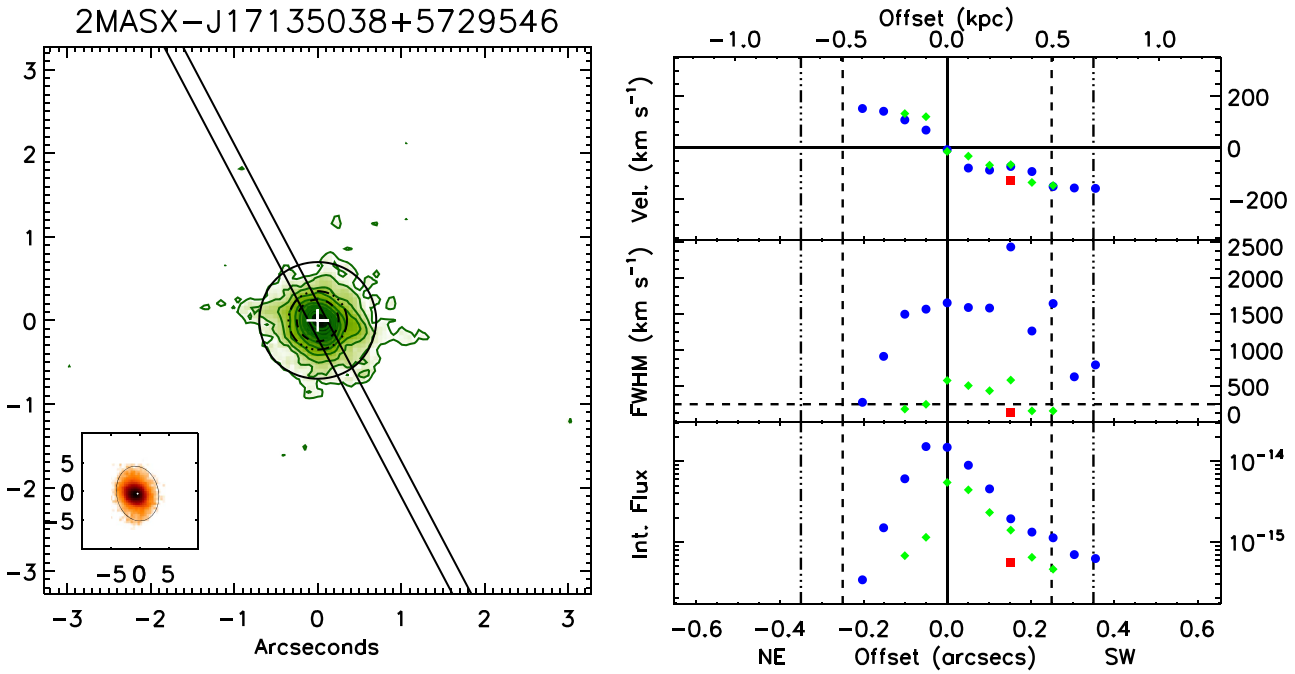

Figure 9. Same as Figure 3 for 2MASX J17135038+5729546. Inset image: the *r*-band SDSS image is 20″ × 20″, with a host disk elliptical fit to 3σ.

in the ENLRs. A smaller value for the slope may simply be due to the absence of gas at large radial distances.

4.2. Extent of Nonrotating Kinematics

In measuring the extent of nonrotating kinematics in our QSO2 sample, we find that the [O III] kinematics observed in Mrk 34 remain exceptionally large, such that the extent of the outflowing gas in this object, $R_{\rm out} = 1.89$ kpc, is ∼75% larger than the next-largest outflow radius in our sample, FIRST J120041.4 at $R_{\rm out} = 1.07$ kpc, and on average, the observed [O III] gas contains radial outflows extending to a distance of ∼0.6 kpc. As Type 2 AGNs have been shown to have systemically lower Eddington ratios than Type 1 AGNs (Ricci et al. 2017), one explanation for the lack of strong, kiloparsec-scale winds in a majority of our sample may be due to low accretion rates. However, our sample contains the most luminous Type 2 AGNs from Reyes et al. (2008) within a redshift of $z < 0.12$, with [O III] luminosities 3–10 times larger than that of Mrk 573. Therefore, it is likely that a majority of our sample is radiating at or near the Eddington limit.

We were not able to determine the bulge radii for the galaxies in our sample to compare to the measured outflow radii because our *HST* continuum images were too shallow to detect the extent of the bulge and the SDSS images are of such scales that the bulges could not be resolved. However, considering that in the case of Mrk 573 the bulge has an effective radius of ∼1 kpc and that most of its mass is enclosed in a ∼2 kpc radius, even if one makes the simplifying assumption that the QSO2s were located in a similar host galaxy, their winds would most likely not be capable of clearing material from the bulge. Similar to our previous findings in Mrk 573, the [O III] outflow radii in our sample are typically a small fraction of the radii encompassing the entire [O III] structures in their host disks. We note that when comparing the radial extent of [O III] emission between imaging and spectroscopy for these QSO2s, spectroscopic measurements only sample the brightest knots of emission observed in imaging for a majority of our targets. However, it is likely that we are observing the majority of radially outflowing kinematics in all of our targets, as outflows are often observed as the brightest knots of AGN-ionized gas, and we observe the kinematics returning from very high velocities or FWHMs by the farthest radial extents of our observations.

As we do not have information on the kinematics of the stellar disks or surrounding molecular hydrogen for these targets to confirm the influence of rotation in our sample, distance measurements reported here are made using the assumption that the observed extended [O III] emission is created via an intersection between ionizing radiation from the central engine and preexisting rotating gas in the host disk. Qualitatively, evidence that the extended, low-velocity gas in these systems is

Table 2
QSO2 Sample SDSS Imaging Measurements

Target	PA_{MA} (degrees)	PA_{diff} (degrees)	R_{MA} (kpc)	e
J07594101	152.0 ± 11.4	49.3	6.5	0.137 ± 0.044
J08025293	111.0 ± 2.2	87.4	6.9	0.254 ± 0.023
MRK 34	29.7 ± 3.1	57.4	13.0	0.246 ± 0.023
J11001238	61.3 ± 1.6	80.7	15.3	0.339 ± 0.016
J115245.66	43.4 ± 5.1	33.3	7.2	0.230 ± 0.040
J120041.4	57.2 ± 7.4	33.1	5.5	0.204 ± 0.047
J13003807	115.8 ± 26.7	48.6	6.9	0.046 ± 0.060
J14054117	91.7 ± 10.7	45.4	7.0	0.128 ± 0.056
B2 1435+30	171.5 ± 7.1	88.6	8.7	0.134 ± 0.035
MRK 477	112.0 ± 9.8	82.2	5.6	0.073 ± 0.023
J16531506	153.0 ± 5.9	77.9	10.6	0.363 ± 0.058
J17135038	191.5 ± 4.6	16.3	9.4	0.238 ± 0.032

Note. Column 2 lists the position angle of the host disk major axis used in our calculations. Column 3 lists the difference between the major axis and STIS long-slit position angles. Columns 4 and 5 list the radius of the major axis and the ellipticity of the host disk used in our measurements, respectively.

Table 3
QSO2 [O III] Imaging Measurements

Target	$PA_{[O\ III]}$ (degrees)	Proj. R_{max} (kpc)	Proj. $R_{90\%}$ (kpc)	3σ F_λ (erg cm^{-2} s^{-1} Å^{-1} pixel^{-1})	Proj. scale	Deproj. R_{max} (kpc)
2MASX J07594101+5050245	105	2.98	0.42	8.8e–20	0.919	3.24
2MASX J08025293+2552551	0	2.76	1.35	8.2e–20	0.768	3.61[a]
MRK 34	150	1.75	1.34	5.3e–20	0.799	2.19
2MASX J11001238+0846157	···	1.98	0.75	7.2e–20	0.661	3.00
SDSS J115245.66+101623.8	10	3.25	1.33	7.4e–20	0.909	3.57
FIRST J120041.4+314745	75	5.92	2.60	5.6e–20	0.974	6.07
2MASX J13003807+5454367	165	4.53	1.58	5.6e–20	0.972	4.66
2MASX J14054117+4026326	···	0.88	0.39	6.3e–20	0.872[a]	1.01
B2 1435+30	90	3.32	1.46	5.9e–20	0.868	3.82
MRK 477	35	2.54	0.83	2.1e–19	0.930	2.74
2MASX J16531506+2349431	77	4.21	1.76	6.6e–20	0.648	6.50
2MASX J17135038+5729546	···	1.38	0.52	5.0e–20	0.762[a]	1.81

Note. Column 4 is the projected radius that encircles 90% of the [O III] flux inside Proj. R_{max}. Column 6 lists the scaling factor used to deproject measurements to their true extents, assuming the observed emission is near the plane of the host galaxy.
[a] Maximum deprojection along the minor axis.

Table 4
QSO2 [O III] Spectroscopic Measurements

Target	Proj. R_{out} (kpc)	Proj. R_{dist} (kpc)	Proj. V_{out} (km s^{-1})	Nuclear FWHM (km s^{-1})	Deproj. R_{out} (kpc)	Deproj. R_{dist} (kpc)	R_{out}/R_{max}
2MASX J07594101+5050245	0.62	0.62	315	1680	0.67	0.67	0.21
2MASX J08025293+2552551	0.44	0.68	−700	870	0.57	0.89	0.08
MRK 34	1.50	1.50	1100	580	1.89	1.89	0.86
2MASX J11001238+0846157	0.45	>1.00	−350	1780	0.68	>1.51	0.23
SDSS J115245.66+101623.8	0.13	>1.12	−300	360	0.15	1.23	0.04
FIRST J120041.4+314745	1.04	>1.55	450	720	1.07	>1.59	0.18
2MASX J13003807+5454367	0.16	0.16	100	580	0.16	0.16	0.04
2MASX J14054117+4026326	0.29	>0.82	100	760	0.33	>0.94	0.33
B2 1435+30	0.17	>1.51	200	630	0.20	>1.74	0.05
MRK 477	0.50	0.84	−500	2040	0.54	0.90	0.20
2MASX J16531506+2349431	0.37	>1.14	110	510	0.57	1.23	0.09
2MASX J17135038+5729546	0.49	>0.70	−160	1660	0.65	>0.92	0.36

Note. Column 2 lists the maximum projected distance of outflowing kinematics. Column 3 lists the maximum projected distance of disturbed kinematics, for gas exhibiting FWHM > 250 km s^{-1} that is at systemic or follows rotation. Column 4 lists the maximum velocity measured inside R_{out} as the maximum outflow velocity. Column 9 lists the ratio of maximum outflow radius to maximum [O III] extent in each target.

in rotation exists in the morphologies of the [O III] regions, as the arc structures observed in several systems resemble spiral arms one would expect to reside in their hosts. Quantitatively, if we compare the difference in position angle between the host major axis and the STIS long-slit observation (PA_{diff}; Table 2), we find that targets with apparent high-amplitude, pronounced rotation curves (i.e., SDSS J115245.66+101623.8 and 2MASX J17135038+5729546) have a smaller PA_{diff}, while targets with higher PA_{diff} (i.e., 2MASX J08025293+2552551 and 2MASX J11001238+0846157) exhibit extended velocities near systemic, suggesting we are sampling rotation in the host disk along the major and minor axes, respectively.

Our findings also agree with similar, recent kinematic studies in nearby, nonmerging QSOs (Liu et al. 2013b; Harrison et al. 2014; McElroy et al. 2015; Karouzos et al. 2016; Villar-Martín et al. 2016; Keel et al. 2017; Ramos Almeida et al. 2017), where maximum outflow distances are measured to be between 1 and 2 kpc, and disrupted gas kinematics are observed out to several kiloparsecs in a majority of targets. These findings suggest that AGNs may still be disrupting gas that would form stars in their host galaxies on bulge-size scales without requiring complete evacuation via outflows.

4.3. [O III] Extent versus [O III] FWHM

The combination of the [O III] images and spectra for the QSO2s in our sample suggests that they can generally be divided into two distinct categories, as shown in Figure 11. Specifically, targets with compact [O III] morphologies tend to exhibit broad nuclear FWHMs (>1500 km s^{-1}), while targets with more extended [O III] morphologies have narrower nuclear FWHMs (<900 km s^{-1}). 2MASX J14054117+4026326 overlaps with both categories, as it has a compact [O III] morphology but also possesses a comparatively small nuclear FWHM of 720 km s^{-1}. We note that in targets with compact morphologies (2MASX J07594101+505245, 2MASX J11001238+0846157, 2MASX J14054117+4026326, 2MASX J17135038+572954, and Mrk 477), the [O III] extent is so compact that we observe the

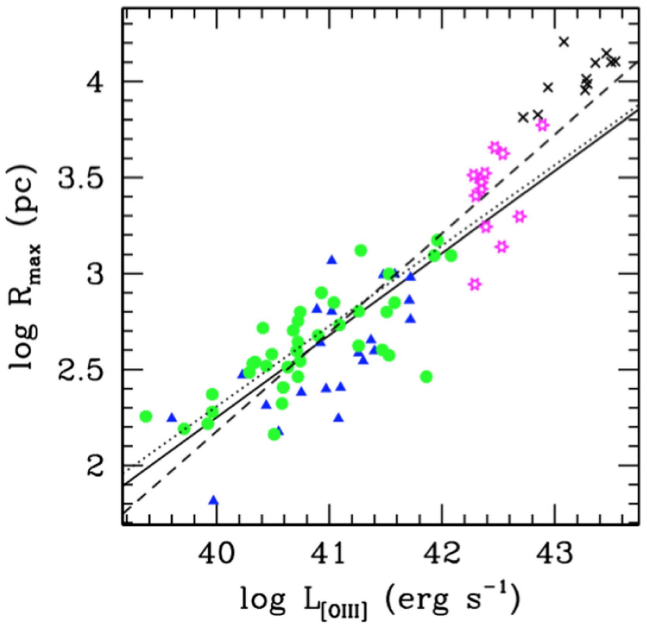

Figure 10. Comparison between projected log R_{max} and log $L_{[O\ III]}$ for Seyfert 1s (blue triangles) and Seyfert 2s (green circles) from Schmitt et al. (2003b), QSO2s (black Xs) from Liu et al. (2013a), and our QSO2s (magenta stars). The best-fitting linear relations obtained using all data (slope = 0.52), only *HST* observations (0.43), or only Seyfert 2 and QSO2 *HST* observations (0.42) are shown as dashed, solid, and dotted lines, respectively.

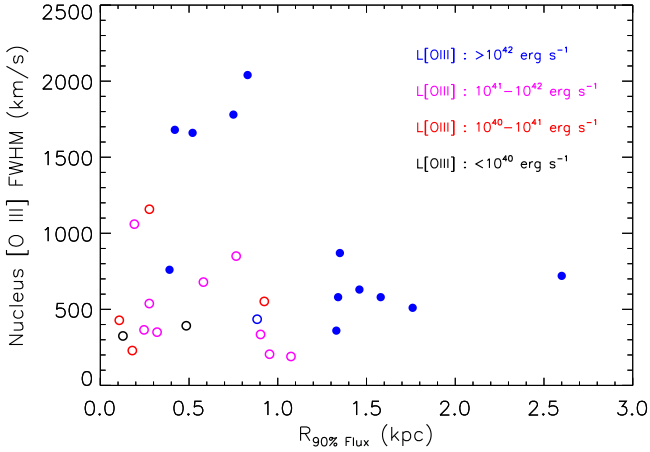

Figure 11. Comparison between the [O III] flux distribution and the maximum nuclear FWHM of each QSO2. Here, $R_{90\%}$ represents the radius that encompasses 90% of the observed [O III] flux in each target inside R_{max}. Solid circles represent measurements from this work. Open circles represent measurements for nearby Type 2 Seyferts from Nelson & Whittle (1995) and Schmitt et al. (2003b).

diffraction spikes typical of a point source in the emission-line images. If this is due to an orientation effect, the compact QSO2s would be viewed roughly face-on, similar to Type 1 AGNs. However, SDSS spectra of these sources show no evidence of hydrogen emission lines being broader than [O III], and the continuum images of these targets (Appendix Figures 13–18) show only the diffuse emission due to the host galaxy and do not show a corresponding nuclear point source that would be expected if these targets were seen face-on. Additionally, other than the broad, central components, the [O III] velocity profiles of the compact sources are generally similar to the extended sources, such as 2MASX J07594101 (Figure 3), compared to FIRST-J12004141 (Figure 4). Therefore, as the compact sources are true Type 2 AGNs, the simplest explanation for the broad [O III] FWHMs is the presence of more material closer to the AGN, with large velocity gradients along our line of sight being produced by high-velocity gas that is outflowing more isotropically. The presence of high-velocity [O III] gas close to the AGN does not necessarily account for the compactness of these sources, as a smaller [O III] morphology in the compact sources could be due to a weaker AGN. However, assuming that [O III] is an isotropic quantity (Heckman et al. 2004), the five compact sources have roughly the same bolometric luminosities as the remaining sources.

The morphological dichotomy that we observe in our QSO2 sample is analogous to what is seen in nearby high-accretion-rate Seyfert galaxies. For example, Figure 12 shows *HST* imaging of [O III] morphologies in the Seyfert 2 galaxies NGC 1068 and Mrk 573 at their observed redshifts, which represent galaxies with broad and narrow [O III] FWHMs, respectively. This figure also shows simulated imaging of what we would expect to observe for the same targets at a redshift of $z = 0.07$, typical of our QSO2 sample. These images were created by resampling the [O III] images of NGC 1068 and Mrk 573 to the expected resolution at $z = 0.07$, and convolving these images with the point-spread function of a corresponding narrow-band filter, to simulate the passage of the image through the telescope optics. The results from this experiment show that in the case of NGC 1068, its [O III] structure is compact enough that if it was placed at a redshift typical of our QSO2s, the [O III] emission would be detected as a point source with fainter line emission surrounding it, similar to what we observe in our compact, high-FWHM targets. Alternatively, in the case of Mrk 573, the resampling and convolution of the image do not cause a significant change to the structure of the [O III] morphology, other than reduced resolution. This is similar to the case of SDSS J115245, a QSO2 with narrow nuclear [O III] FWHM measurements.

A possible explanation for the difference in morphology is that there is more gas close to the AGN in the compact targets, which results in the attenuation of a fraction of ionizing radiation. STIS observations of NGC 1068 support this idea, as they reveal bright nuclear [O III] emission with FWHM $>$ 1000 km s^{-1} (Crenshaw & Kraemer 2000; Das et al. 2006). A photoionization analysis of these observations, performed by Kraemer & Crenshaw (2000), suggested that the observed ionizing radiation is attenuated by gas close to the AGN. Additionally, the scattered optical continuum is centrally peaked (Crenshaw & Kraemer 2000), and, based on *Chandra*/ACIS imaging, the X-ray source is $\lesssim$165 pc in extent (Young et al. 2001). Therefore, all of this together indicates there is a large concentration of ionized gas at small radii (100–200 pc).

It is unlikely that the optical emission-line gas is attenuating much of the ionizing radiation, since, based on our studies of Seyfert galaxies (Kraemer & Crenshaw 2000; Collins et al. 2009), the [O III] gas has a small covering factor. On the other hand, X-ray emission-line gas in the NLR can possess covering factors close to unity (e.g., Kraemer et al. 2015). As the medium responsible for the scattering and polarization of the hidden broad-line emission lines and continuum in Type 2 AGNs must possess large covering factors and column densities (Antonucci 1993), it is possible that the ionizing radiation has been attenuated by absorption or scattering in high-ionization gas. Note, however, that strong, soft X-ray emission lines would be formed in the attenuating medium, assuming that elements such as O, N, C, and Ne are not fully ionized.

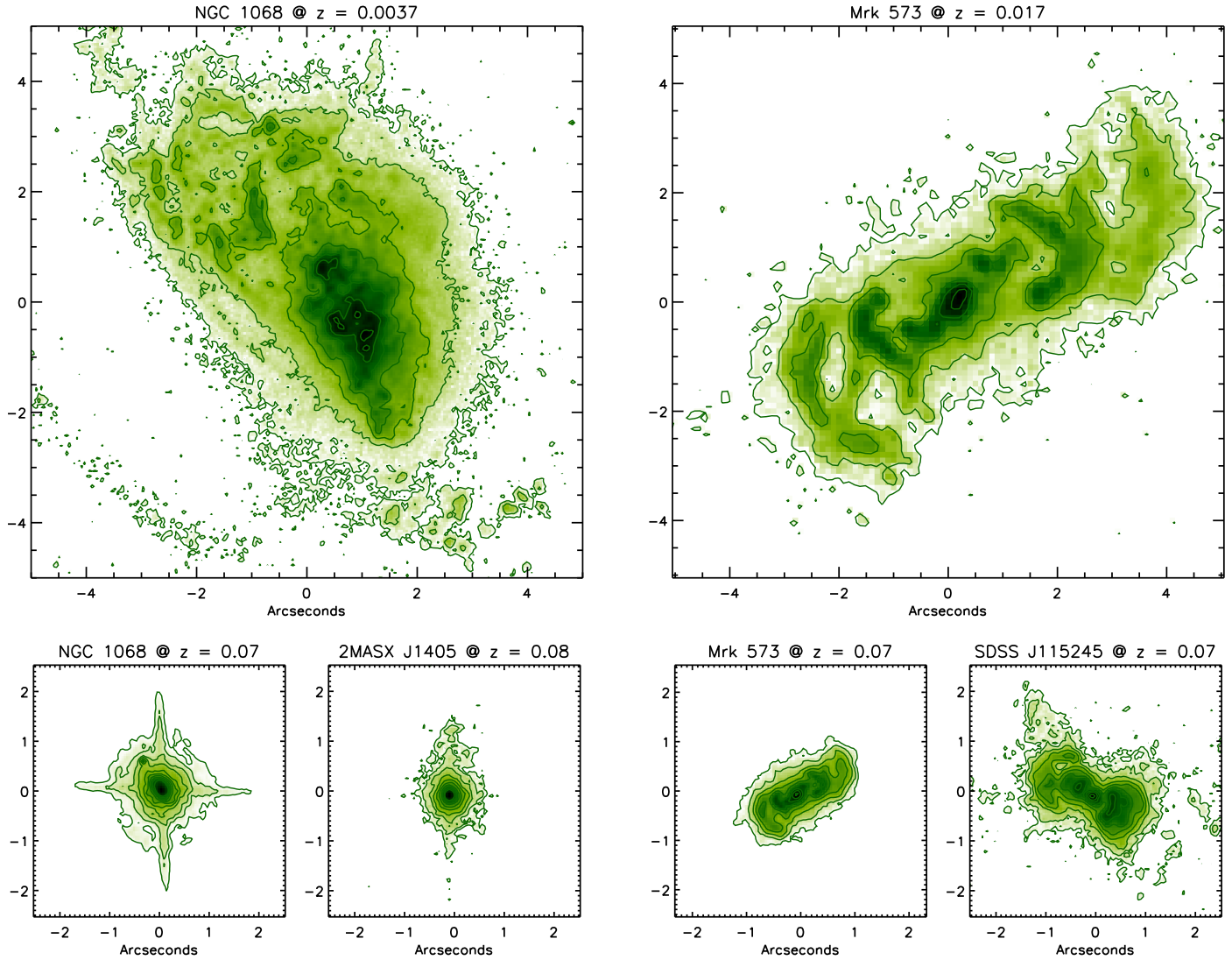

Figure 12. Top: archival *HST*/WFPC2 [O III] images of NGC 1068 and Mrk 573. Bottom: comparisons between archival *HST* [O III] images of NGC 1068 and Mrk 573, resampled to simulate being located at $z \sim 0.07$ and convolved with the point-spread function of ACS using the F502N filter, and *HST*/ACS images of 2MASX J140541 and SDSS J115245 at comparable redshifts. High concentrations of [O III] flux in the nucleus of NGC 1068 at $z = 0.07$ produce diffraction spikes, similar to the compact sources in our QSO2 sample.

Given the evidence for strong outflows in NGC 1068 (Das et al. 2005) and that it is likely radiating near Eddington (Kraemer et al. 2015), this gas could eventually be driven away from the inner nucleus. This would reduce the amount of emission-line gas at small radial distances, which would weaken or eliminate the broad [O III]. This also could drive out the X-ray emission-line gas, which would reduce the attenuation of the ionizing radiation, resulting in a more extended [O III] structure. As such, it may be that the compact QSO2s are in a similar state and that a transition occurs from compact AGNs, with higher central concentrations of gas, to the more extended sources observed in the remainder of our sample, which resemble Mrk 573 with extended morphologies and nuclear FWHMs on the scale of hundreds of $\mathrm{km\,s^{-1}}$ (Fischer et al. 2010, 2017).

5. Conclusions

We have analyzed the [O III] morphology and emission-line kinematics of a sample of 12 QSO2s via high-resolution imaging and spectroscopy with *HST*. Our major findings are as follows:

(1) Our targets consist of several of the most luminous Type 2 AGNs within a redshift of $z = 0.12$, yet [O III] morphologies in our sample vary from compact, core-like structures to extended structures, all several kiloparsecs in length. Overall, the size of [O III] regions scales with luminosity in comparison to nonmerging Seyfert galaxies and QSO2s observed to similar sensitivities.

(2) Radially outflowing kinematics exist in all of our targets, with maximum outflow distances ranging between 150 and 1890 pc and a mean $R_{\rm out}$ of ~600 pc. The extents of these outflows are relatively small compared to the overall extent of the [O III] morphology, with an average $R_{\rm out}/R_{\rm max} = 0.22$. As such, our findings suggest that a majority of observed extended [O III] emission is often in rotation and not driven radially by AGN winds, questioning the effectiveness of AGNs being capable of clearing material from their host bulge in the nearby universe.

(3) A majority of our sample also show signatures of gas at systemic velocity or following rotation that is disturbed by the central AGN (FWHM $> 250\,\mathrm{km\,s^{-1}}$) at distances outside the maximum measured radial outflow radii, with maximum radii ranging from 160 to 1860 pc, with a mean $R_{\rm dist}$ of ∼1130 pc. These findings suggest that AGN activity may be disrupting gas that forms stars without requiring complete evacuation.
(4) We find our targets fall into two classes when comparing [O III] radial extent and nuclear FWHM, such that QSO2s with a more compact [O III] morphology have broader nuclear emission lines. We hypothesize that this could be due to a transitional effect, where QSO2s with compact morphologies possess comparatively large amounts of gas near the AGN, which may be driven out at later states.

This research has made use of the NASA/IPAC Extragalactic Database (NED), which is operated by the Jet Propulsion Laboratory, California Institute of Technology, under contract with the National Aeronautics and Space Administration.

Funding for the Sloan Digital Sky Survey IV has been provided by the Alfred P. Sloan Foundation, the U.S. Department of Energy Office of Science, and the Participating Institutions. SDSS-IV acknowledges support and resources from the Center for High-Performance Computing at the University of Utah. The SDSS web site is http://www.sdss.org.

SDSS-IV is managed by the Astrophysical Research Consortium for the Participating Institutions of the SDSS Collaboration including the Brazilian Participation Group, the Carnegie Institution for Science, Carnegie Mellon University, the Chilean Participation Group, the French Participation Group, Harvard-Smithsonian Center for Astrophysics, Instituto de Astrofísica de Canarias, The Johns Hopkins University, Kavli Institute for the Physics and Mathematics of the Universe (IPMU)/University of Tokyo, Lawrence Berkeley National Laboratory, Leibniz Institut für Astrophysik Potsdam (AIP), Max-Planck-Institut für Astronomie (MPIA Heidelberg), Max-Planck-Institut für Astrophysik (MPA Garching), Max-Planck-Institut für Extraterrestrische Physik (MPE), National Astronomical Observatories of China, New Mexico State University, New York University, University of Notre Dame, Observatário Nacional/MCTI, The Ohio State University, Pennsylvania State University, Shanghai Astronomical Observatory, United Kingdom Participation Group, Universidad Nacional Autónoma de México, University of Arizona, University of Colorado Boulder, University of Oxford, University of Portsmouth, University of Utah, University of Virginia, University of Washington, University of Wisconsin, Vanderbilt University, and Yale University.

The authors thank the anonymous referee for their helpful comments that improved the clarity of this work. T.C.F. was supported by an appointment to the NASA Postdoctoral Program at the NASA Goddard Space Flight Center, administered by Universities Space Research Association under contract with NASA. Basic research at the Naval Research Laboratory is funded by 6.1 base funding. M.R. gratefully acknowledges support from the National Science Foundation through the Graduate Research Fellowship Program (DGE-1550139). L.C.H. was supported by the National Key R&D Program of China (2016YFA0400702) and the National Science Foundation of China (11473002, 11721303). M.V. gratefully acknowledges financial support from the Danish Council for Independent Research via grant DFF 4002-00275.

Appendix
Individual Target Descriptions

A.1. 2MASX J075941

The [O III] structure in this target is highly asymmetric, with faint, extended knots of emission to the east of the nucleus. Kinematics are obtained near the nucleus (total extent $<1''$), with a two-component emission line (FWHMs of ∼1500 and $100\,\mathrm{km\,s^{-1}}$) observed near systemic throughout, and intermediate-width components (FWHM $\sim 500\,\mathrm{km\,s^{-1}}$) traveling in different directions on either side of the nucleus inside 500 pc. We measure the maximum extent of these kinematics as the observed outflow radius $R_{\rm out} = 620$ pc. At greater distances, we measure single-component emission lines at systemic with FWHMs $< 250\,\mathrm{km\,s^{-1}}$, which we define as undisturbed rotation. As such, we do not measure a distinct disturbed kinematics maximum radius, $R_{\rm dist}$ in this target. This QSO resides in a relatively face-on system that does not have any companions or tidal tails, suggesting no recent galaxy interaction activity.

A.2. 2MASX J080252

This QSO has an asymmetric, conical [O III] morphology pointing north of the nucleus. Kinematics are obtained from the nucleus to distances >1 kpc north, with emission-line fluxes rapidly becoming fainter south of the nucleus, consistent with the opposite cone being extinguished by the host disk. Rapid differences in FWHM and velocity between nucleus and immediately off-nucleus measurements are due to blending of the blueshifted, offset component, as seen in Figure 2, at off-nuclear positions. Here, $R_{\rm out}$ is measured as the extent of the multicomponent emission lines, which extend along the STIS slit to the northeast approximately 500 pc. Single-component, broad FWHM ($>250\,\mathrm{km\,s^{-1}}$) emission lines near systemic are observed to extend to an additional 200 pc, for an $R_{\rm dist}$ of ∼700 pc. Emission lines at greater radii to the northeast have a single narrow ($<250\,\mathrm{km\,s^{-1}}$) component that suggests that the gas is kinematically undisrupted. This target resides in a host that has recently experienced some galaxy interaction, with a long tidal tail extending 15″ east of the system. Elliptical fits to this system result in a highly inclined disk, which may be affected by the resultant morphology.

A.3. Mrk 34

The [O III] morphology in Mrk 34 is a clear biconical structure, with a "Z" shape likely due to the illumination of spiral arms in the host disk, similar to previously observed targets like Mrk 3 (Crenshaw et al. 2010) and Mrk 573 (Fischer et al. 2010, 2017). [O III] kinematics across the three separate slit positions show high-velocity ($\sim 1000\,\mathrm{km\,s^{-1}}$) outflows existing inside projected distances of 500 pc. Extended kinematics for the rest of the system appear to be largely rotational, but large deviations from rotation and emission-line splitting are present on either end of the nucleus out to ∼1.5 kpc. Here, we observe line splitting with both lines deviating from the rotation curve in opposite directions, to an

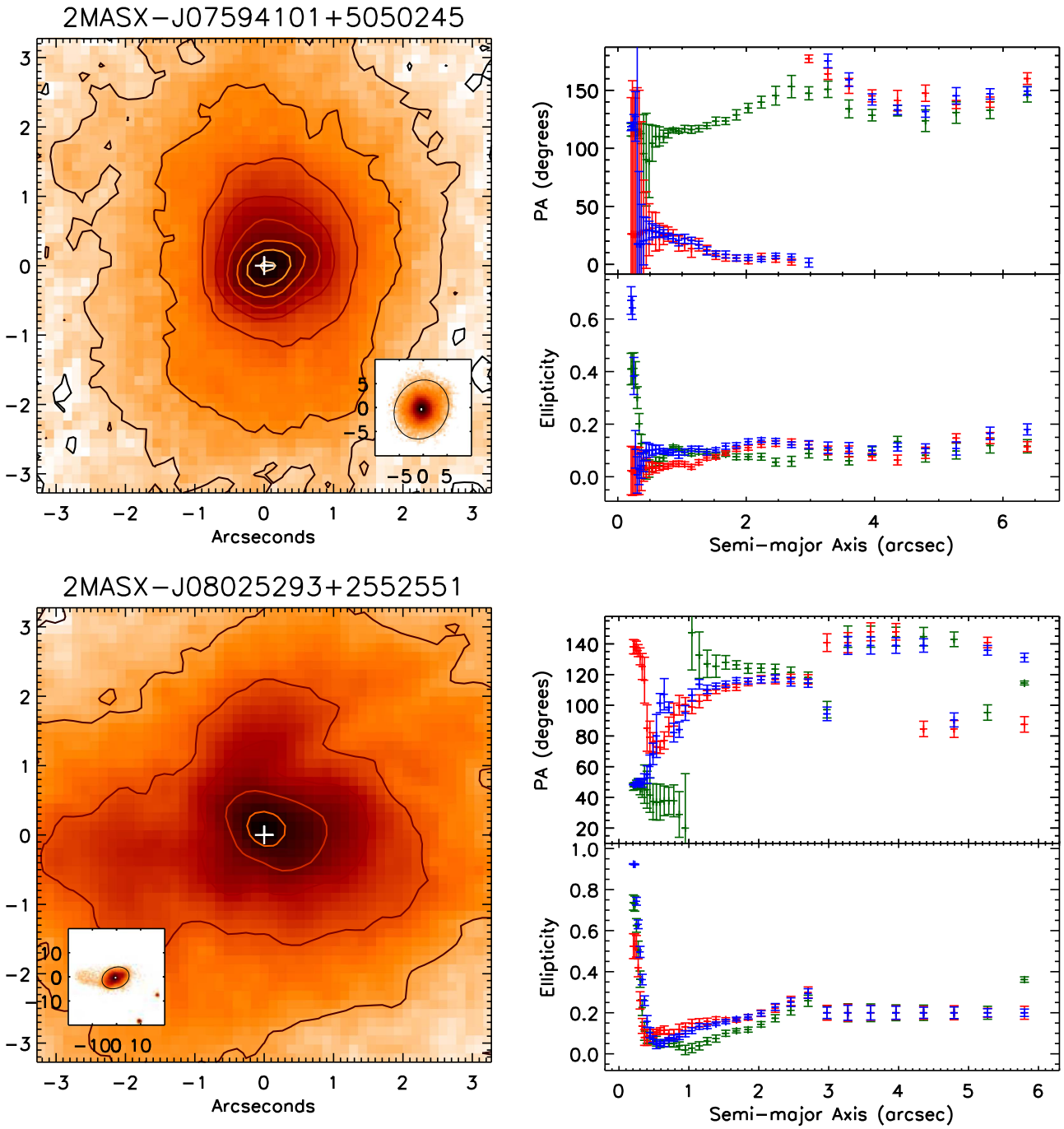

Figure 13. *HST* and SDSS data sets for 2MASX J07594101+505245 and 2MASX J08025293+2552551. Left: The large window presents 5″ × 5″ continuum images of each target. Flux contours start at 3σ over background and increase in powers of 2 times 3σ (i.e., 3$\sigma \times 2^n$). The position of the nucleus, measured at the flux peak of each target, is plotted as a white cross. The inset image displays a zoomed-out continuum *r*-band SDSS image of the target host galaxy with the outermost elliptical fit overplotted. Right: position angle and ellipticity outputs of elliptical fits to SDSS *g*- (green), *r*- (red), and *i*-band (blue) imaging out to a 3σ detection for 2MASX J07594101+505245 and 5σ for 2MASX J08025293+2552551.

approximate maximum difference of 500 km s^{-1}. Regions that display line splitting are observed as the outer arcs being illuminated in the NLR, suggesting that these kinematics are due to material in the spiral arms being driven or ablated in directions perpendicular to the radial outflows. We define $R_{\rm out}$ to encompass the entirety of the observed kinematics with multiple components for a radial distance of 1.50 kpc. This distance also marks the extent of $R_{\rm dist}$, as kinematics at greater radii follow a likely rotation pattern and have FWHM measurements of approximately 250 km s^{-1}. The host galaxy of Mrk 34 is a well-resolved spiral galaxy that is moderately inclined with no evidence of merger activity.

Mrk 34 has been studied significantly more than a majority of our targets. VLA radio observations (Falcke et al. 1998) show a radio jet structure well aligned with the optical ionized-gas morphology, where radio hot spots coincide with regions of low excitation. *NuSTAR* 3–40 keV observations by Gandhi et al. (2014) found that Mrk 34 is the nearest nonmerging, Compton-thick QSO2, with soft X-ray emission being driven by AGN photoionization versus star formation. This follows

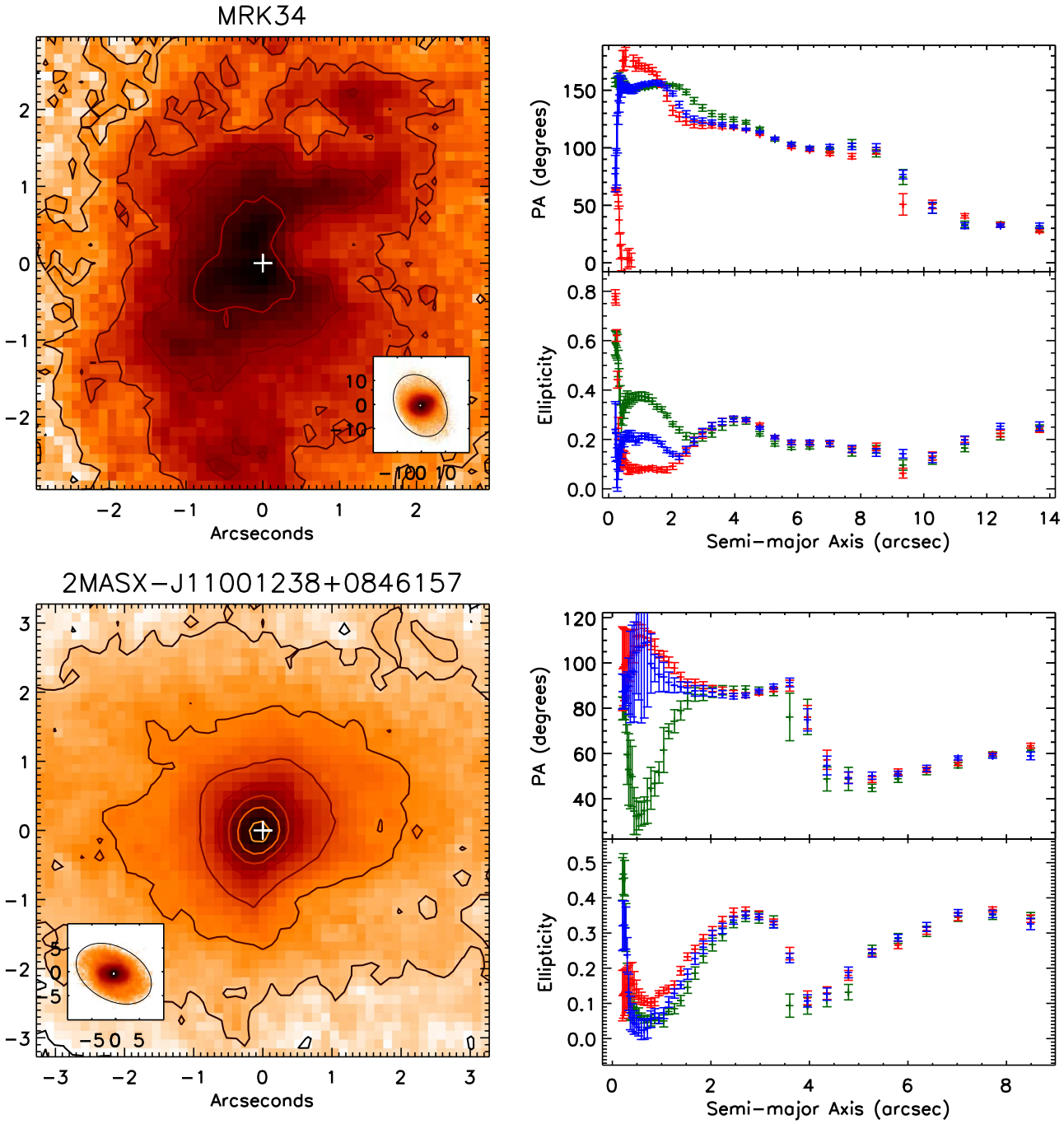

Figure 14. Same as Figure 13 for Mrk 34 and SDSS J115245.66+101623.8. Host disk ellipticals are both fit to 3σ.

the findings that Mrk 34 lacks nuclear star formation (González Delgado et al. 2001; Stoklasová et al. 2009), which may be suppressed by AGN feedback (Wang et al. 2007).

A.4. 2MASX J110012

This target has a compact [O III] morphology, which is nearly circular with diffraction spikes and a slight extension to the southeast. High-FWHM emission (>1000 km s^{-1}) is measured across the nucleus and is blueshifted to the southeast. We measure $R_{\rm out}$ to the maximum extent of these high-FWHM measurements at 450 pc northwest of the nucleus. Disturbed kinematics extend to the farthest observations northwest of the nucleus, $R_{\rm dist} = 1$ kpc, where we measure single-component emission lines at systemic with widths of ~500 km s^{-1}, which may be a product of blending multiple components as observed over the nucleus. This QSO2 resides in a well-resolved barred spiral galaxy that is moderately inclined with no evidence of recent interactions or ongoing mergers.

A.5. SDSS J115245

This target has a clear biconical [O III] morphology, with arcs of emission that suggest that a majority of the gas exists in illuminated spiral arms. The observed kinematics appear to be largely rotational, with redshifted rotation to the north and blueshifted rotation to the south. High peak rotation velocities (~200 km s^{-1}) are consistent with the alignment between the

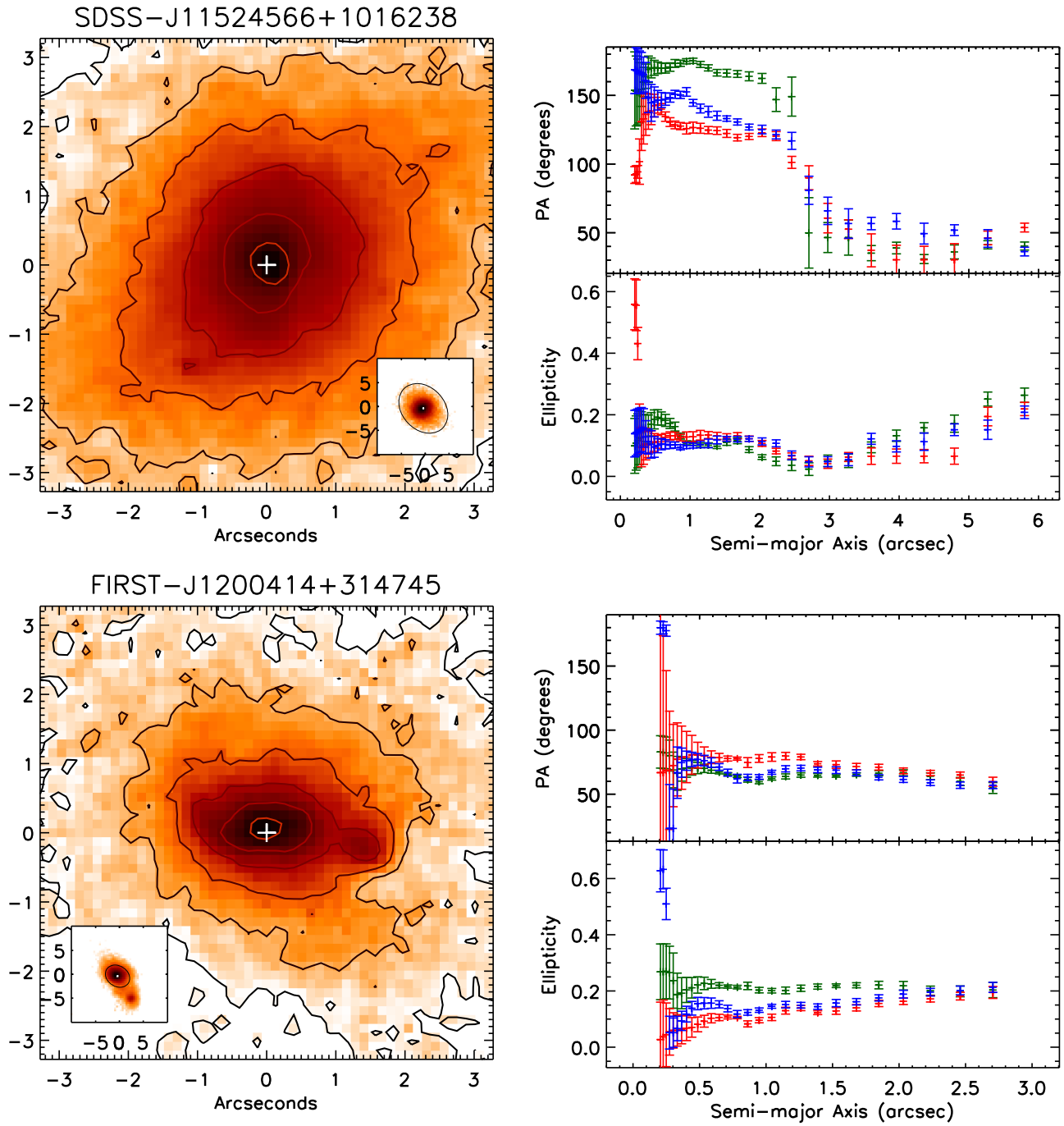

Figure 15. Same as Figure 13 for SDSS J115245.66+101623.8 and FIRST J120041.4+314745. Host-disk elliptical fits are to 3σ and 9σ, respectively.

modeled host major axis and STIS long-slit position angles ($PA_{diff} = 33.^{\circ}3$). Narrow emission-line components are measured going opposite to the direction of rotation immediately northeast of the nucleus and represent the extent of outflows with $R_{out} = 130$ pc. Also, ~400 km s^{-1} FWHM gas is observed in rotation at radii outside the first northern arc of emission, for an R_{dist} of ~1.1 kpc. The host galaxy for this target is moderately inclined with no signs of recent interaction activity.

A.6. FIRST J120041

FIRST J120041 has the largest projected [O III] morphology extent in our sample, with an R_{max} of ~6 kpc, which is on the same scale as the extent of the observable host galaxy in SDSS imaging. [O III] velocities are measured on much smaller scales, extending to distances between 0.8 and 1.5 kpc from the nucleus, which can be mapped to the two bright lobes on either side of the nucleus along the STIS slit. Multicomponent and high-velocity emission lines are observed in the inner 0.″5, for an R_{out} of ~1 kpc, with high-FWHM, single-component emission lines detected to the farthest extent of our measurements ($R_{dist} = 1.12$ kpc). Outflows and disturbed kinematics may reach to farther distances outside the area sampled by the STIS slit, as the bright knots where we observe the high-velocity gas extend to a radius of ~0.″76, or ~1.55 kpc. This target appears to be part of an ongoing or recent interaction with a smaller satellite galaxy to the southwest, as filamentary structure can be observed linking the two systems.

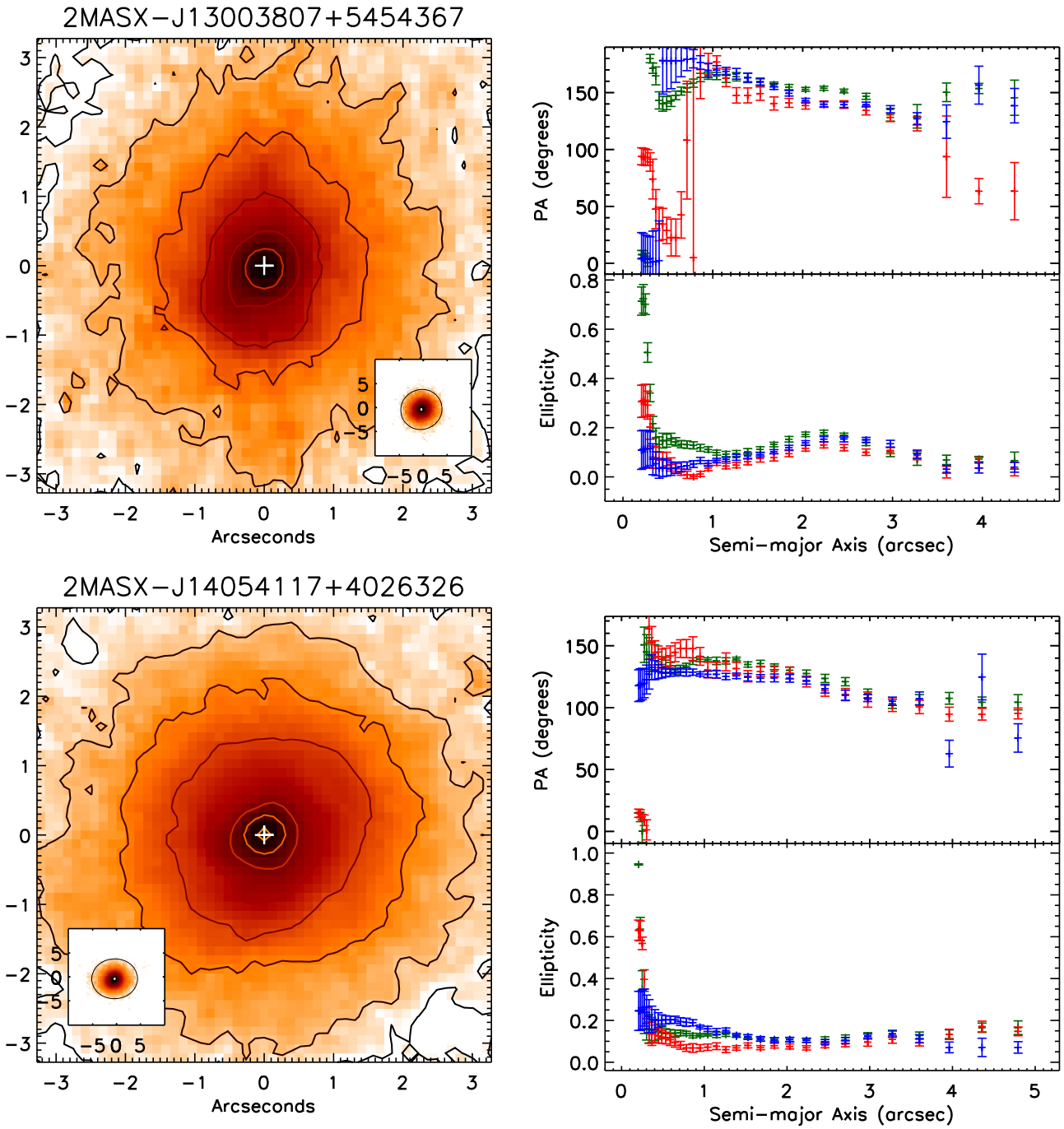

Figure 16. Same as Figure 13 for 2MASX J13003807+5454367 and 2MASX J14054117+4026326. Host disk elliptical fits are both to 3σ.

A.7. 2MASX J130038

The [O III] structure of this target is extended, with two arcs of bright emission and a linear feature near the nucleus, suggesting that the observed morphology is due to spiral arms being illuminated by the central engine. The kinematics sampled by our STIS observations agree with this interpretation, as they appear to be largely in kinematically undisturbed rotation. Velocities are blueshifted to the southeast and redshifted to the northwest, with FWHMs ranging between 100 and 200 km s^{-1}. A compact, broad FWHM component is observed immediately northwest of the nucleus, with $R_{\rm out} \sim 160$ pc, suggesting outflows are being driven off the linear filament near the nucleus observed in imaging, similar to Mrk 573. As single-component emission lines at greater radii possess FWHMs < 250 km s^{-1}, $R_{\rm out}$ and $R_{\rm dist}$ are the same distance. The host of this QSO2 appears to be relatively face-on without any signs of recent interactions.

A.8. 2MASX J140541

This source has a compact [O III] morphology. The measured $R_{\rm max}$ is inside the observed [O III] morphology as it is artificially extended by diffraction spikes. The kinematics show the gas to be near systemic, with slightly blueshifted outflows over the nucleus possessing FWHMs of $\sim$800 km s^{-1} out to an $R_{\rm out} \sim 300$ pc. FWHM measurements remain near 400 km s^{-1} for single-component emission lines at the farthest extent

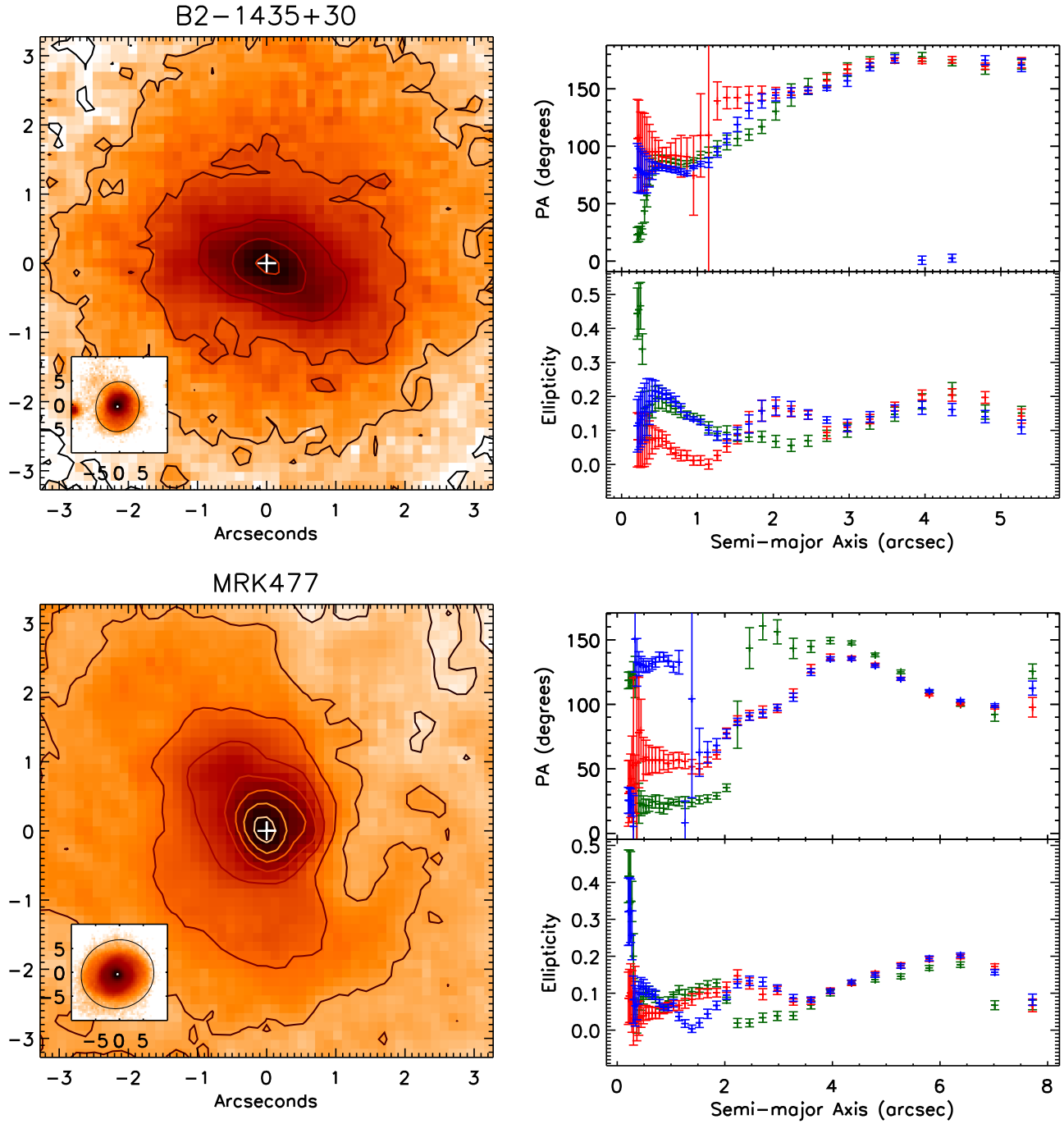

Figure 17. Same as Figure 13 for B2 1435+30 and Mrk 477. Host disk ellipticals are fit to 5σ for both targets.

of our measurements, suggesting kinematically disturbed gas exists throughout ($R_{\rm dist} \sim 850$ pc). The farther extension of gas kinematics to the northwest suggests that the host disk may be extinguishing emission to the southeast. The host is moderately inclined, without signs of recent interaction activity.

A.9. B2 1435+30

The [O III] morphology of B2 1435+30 is biconical, with a compact arc to the east and a bright, extended cone to the west, which are both traced kinematically by our STIS observations. This target does not possess significantly high velocities or multiple components in its kinematics; however, we find that the redshifted, high-FWHM ($\sim$700 km s^{-1}) gas kinematics over the nucleus do not follow the overall rotation pattern of the surrounding gas at greater radii, and we deem these kinematics to be in outflow, with $R_{\rm out} = 170$ pc. Kinematics across the features outside the nucleus resemble kinematically disturbed rotation, observed as 400 km s^{-1} FWHM gas, extending throughout the southwest cone, with $R_{\rm dist} > 1.5$ kpc. This target appears to be part of a recent galaxy interaction, with extended structure in SDSS imaging linking it to an eastern satellite galaxy.

A.10. Mrk 477

The [O III] morphology of this target is largely composed of two emission-line knots inside 500 pc, with fainter emission extending to radii of $\sim$2.5 kpc. [O III] kinematics suggest that

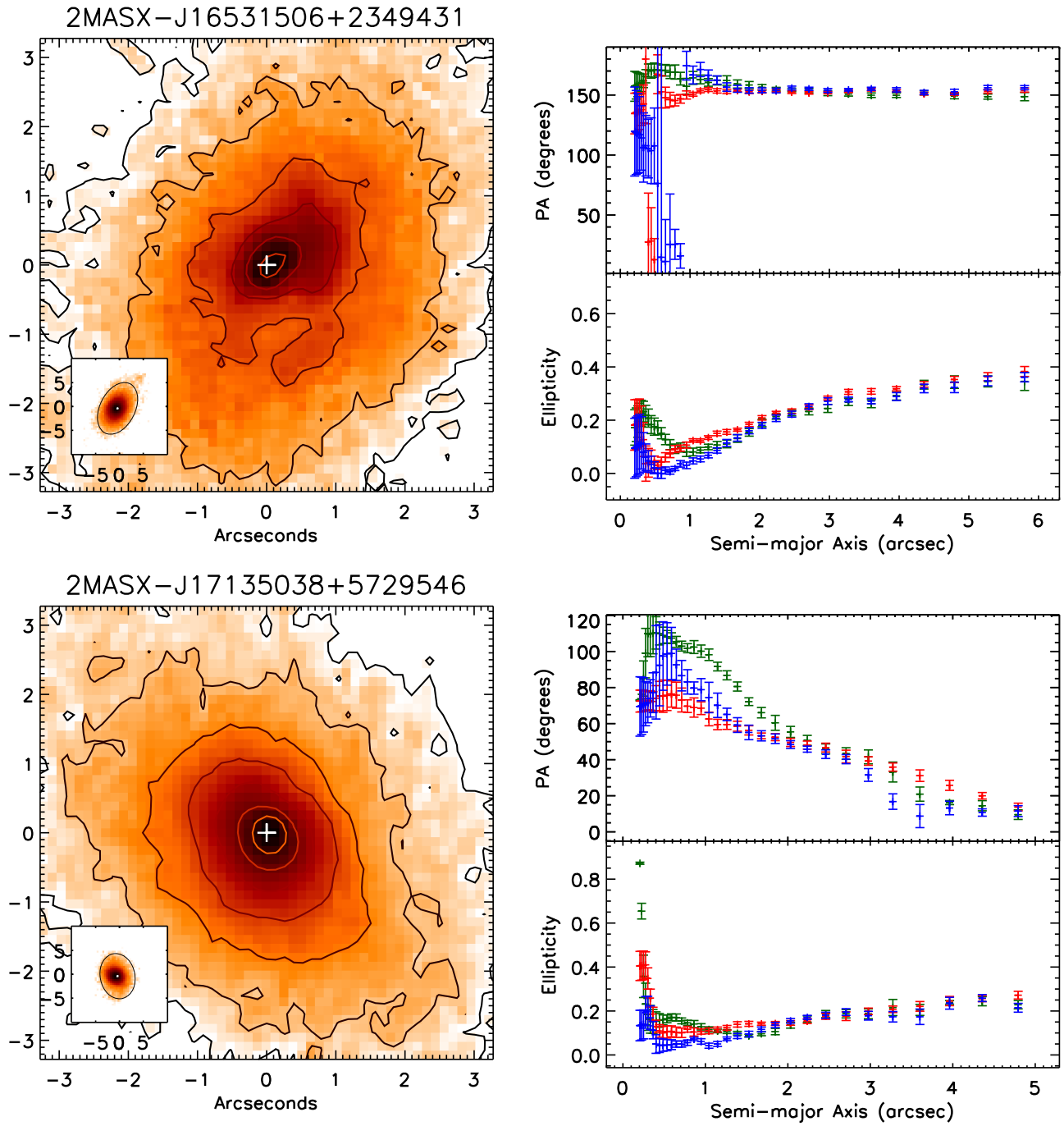

Figure 18. Same as Figure 13 for 2MASX J16531506+2349431 and 2MASX J17135038+5729546. Host disk ellipticals are fit to 3σ for both targets.

the gas is largely in rotation near systemic, with additional emission over the nucleus extending to radii ∼500 pc that displays multiple emission-line components and excessively large FWHMs ∼2000 km s^{-1}. Relatively moderate FWHM (>500 km s^{-1}), single-component, near-systemic emission-line kinematics extend to farther distances of $R_{\rm dist}$ = 840 pc. This target resides in a well-resolved spiral galaxy that shows signs of a recent interaction in tidal streams that bridge Mrk 477 to neighboring galaxies to the northeast (De Robertis 1987).

Similar to Mrk 34, Mrk 477 is also well studied. UV through near-IR analyses by Heckman et al. (1997) show that a large portion of the energetics in this system is provided by an ongoing, compact nuclear starburst in this target. Radio emission at 8.4 GHz extends to a radius of ∼500 pc along a position angle ∼30°, similar to our STIS long-slit position.

A.11. 2MASX J165315

The [O III] morphology in this target is distributed in three features: a faint arc ∼4 kpc east of the nucleus, a central lobe extending east from the nucleus, and a fan or conical shape west of the nucleus. [O III] kinematics are only obtained for the central lobe and western fan, with a largely rotational pattern. The maximum outflow radius is defined by a relatively broad (>500 km s^{-1}) and systemic (or blueshifted with respect to the narrow component) secondary component observed east of the nucleus for an $R_{\rm out}$ = 370 pc. Single-component

line emission with FWHM $> 250\,\mathrm{km\,s^{-1}}$ that follows a low-amplitude rotation pattern is measured throughout the rest of the system, for an R_{dist} of 1.1 kpc. The host galaxy of this target is moderately inclined, with no signs of a recent merger.

A.12. 2MASX J171350

Similar to 2MASX J140541, this source has a compact [O III] morphology, and the measured R_{max} is inside the observed [O III] morphology as it is artificially extended by diffraction spikes. The kinematics in this system follow a rotation pattern, redshifted to the northeast and blueshifted to the southwest, with broad emission-line FWHMs frequently around $1500\,\mathrm{km\,s^{-1}}$. High peak rotation velocities ($\sim 200\,\mathrm{km\,s^{-1}}$) are consistent with the alignment between the modeled host major axis and STIS long-slit position angles ($\mathrm{PA_{diff}} = 16\overset{\circ}{.}3$). Multicomponent emission lines are observed out to 490 pc, which we define as R_{out}. Blending of these components likely occurs in measurements near the ends of our STIS observations, with the very broad component becoming too faint to individually detect at a 3σ level, creating a single-component emission line possessing disturbed kinematics that extends to an R_{dist} of $\sim$700 pc. The host is moderately inclined, without signs of a recent merger.

ORCID iDs

Travis C. Fischer https://orcid.org/0000-0002-3365-8875
S. B. Kraemer https://orcid.org/0000-0002-6928-9848
D. M. Crenshaw https://orcid.org/0000-0002-6465-3639
M. Revalski https://orcid.org/0000-0002-4917-7873
M. Vestergaard https://orcid.org/0000-0001-9191-9837
M. Elvis https://orcid.org/0000-0001-5060-1398
C. M. Gaskell https://orcid.org/0000-0003-4888-2009
L. C. Ho https://orcid.org/0000-0001-6947-5846
R. Mushotzky https://orcid.org/0000-0002-7962-5446
H. Netzer https://orcid.org/0000-0002-6766-0260
T. Storchi-Bergmann https://orcid.org/0000-0003-1772-0023
T. J. Turner https://orcid.org/0000-0003-2971-1722

References

Antonucci, R. 1993, ARA&A, 31, 473
Bae, H.-J., & Woo, J.-H. 2016, ApJ, 828, 97
Bellocchi, E., Arribas, S., Colina, L., & Miralles-Caballero, D. 2013, A&A, 557, A59
Bennert, N., Falcke, H., Schulz, H., Wilson, A. S., & Wills, B. J. 2002, ApJL, 574, L105
Buchner, J., Georgakakis, A., Nandra, K., et al. 2014, A&A, 564, A125
Cicone, C., Maiolino, R., Sturm, E., et al. 2014, A&A, 562, A21
Collins, N. R., Kraemer, S. B., Crenshaw, D. M., Bruhweiler, F. C., & Meléndez, M. 2009, ApJ, 694, 765
Crenshaw, D. M., & Kraemer, S. B. 2000, ApJL, 532, L101
Crenshaw, D. M., & Kraemer, S. B. 2005, ApJ, 625, 680
Crenshaw, D. M., & Kraemer, S. B. 2012, ApJ, 753, 75
Crenshaw, D. M., Kraemer, S. B., & George, I. M. 2003, ARA&A, 41, 117
Crenshaw, D. M., Kraemer, S. B., Schmitt, H. R., et al. 2010, AJ, 139, 871
Das, V., Crenshaw, D. M., Hutchings, J. B., et al. 2005, AJ, 130, 945
Das, V., Crenshaw, D. M., Kraemer, S. B., & Deo, R. P. 2006, AJ, 132, 620
De Robertis, M. M. 1987, ApJ, 316, 597
Eisenstein, D. J., Weinberg, D. H., Agol, E., et al. 2011, AJ, 142, 72
Falcke, H., Wilson, A. S., & Simpson, C. 1998, ApJ, 502, 199
Feroz, F., & Hobson, M. P. 2008, MNRAS, 384, 449
Feroz, F., Hobson, M. P., & Bridges, M. 2009, MNRAS, 398, 1601
Feroz, F., Hobson, M. P., Cameron, E., & Pettitt, A. N. 2013, arXiv:1306.2144
Fischer, T. C., Crenshaw, D. M., Kraemer, S. B., & Schmitt, H. R. 2013, ApJS, 209, 1
Fischer, T. C., Crenshaw, D. M., Kraemer, S. B., Schmitt, H. R., & Trippe, M. L. 2010, AJ, 140, 577
Fischer, T. C., Crenshaw, D. M., Kraemer, S. B., Schmitt, H. R., & Turner, T. J. 2014, ApJ, 785, 25
Fischer, T. C., Machuca, C., Diniz, M. R., et al. 2017, ApJ, 834, 30
Gandhi, P., Lansbury, G. B., Alexander, D. M., et al. 2014, ApJ, 792, 117
Ganguly, R., & Brotherton, M. S. 2008, ApJ, 672, 102
Genzel, R., Förster Schreiber, N. M., Rosario, D., et al. 2014, ApJ, 796, 7
González Delgado, R. M., Heckman, T., & Leitherer, C. 2001, ApJ, 546, 845
Greene, J. E., Zakamska, N. L., Ho, L. C., & Barth, A. J. 2011, ApJ, 732, 9
Greene, J. E., Zakamska, N. L., & Smith, P. S. 2012, ApJ, 746, 86
Harrison, C. M., Alexander, D. M., Mullaney, J. R., & Swinbank, A. M. 2014, MNRAS, 441, 3306
Heckman, T. M., González-Delgado, R., Leitherer, C., et al. 1997, ApJ, 482, 114
Heckman, T. M., Kauffmann, G., Brinchmann, J., et al. 2004, ApJ, 613, 109
Hopkins, P. F., Hernquist, L., Cox, T. J., et al. 2005, ApJ, 630, 705
Karouzos, M., Woo, J.-H., & Bae, H.-J. 2016, ApJ, 819, 148
Keel, W. C., Lintott, C. J., Maksym, W. P., et al. 2017, ApJ, 835, 256
Khalatyan, A., Cattaneo, A., Schramm, M., et al. 2008, MNRAS, 387, 13
King, A., & Pounds, K. 2015, ARA&A, 53, 115
Kormendy, J., & Ho, L. C. 2013, ARA&A, 51, 511
Kraemer, S. B., & Crenshaw, D. M. 2000, ApJ, 544, 763
Kraemer, S. B., Sharma, N., Turner, T. J., George, I. M., & Crenshaw, D. M. 2015, ApJ, 798, 53
Liu, G., Zakamska, N. L., Greene, J. E., Nesvadba, N. P. H., & Liu, X. 2013a, MNRAS, 430, 2327
Liu, G., Zakamska, N. L., Greene, J. E., Nesvadba, N. P. H., & Liu, X. 2013b, MNRAS, 436, 2576
McElroy, R., Croom, S. M., Pracy, M., et al. 2015, MNRAS, 446, 2186
Mullaney, J. R., Alexander, D. M., Fine, S., et al. 2013, MNRAS, 433, 622
Müller-Sánchez, F., Prieto, M. A., Hicks, E. K. S., et al. 2011, ApJ, 739, 69
Nelson, C. H., & Whittle, M. 1995, ApJS, 99, 67
Nevin, R., Comerford, J., Müller-Sánchez, F., Barrows, R., & Cooper, M. 2016, ApJ, 832, 67
Rafter, S. E., Crenshaw, D. M., & Wiita, P. J. 2009, AJ, 137, 42
Ramos Almeida, C., Piqueras López, J., Villar-Martín, M., & Bessiere, P. S. 2017, MNRAS, 470, 964
Reyes, R., Zakamska, N. L., Strauss, M. A., et al. 2008, AJ, 136, 2373
Ricci, C., Trakhtenbrot, B., Koss, M. J., et al. 2017, Natur, 549, 488
Schmitt, H. R., Donley, J. L., Antonucci, R. R. J., et al. 2003a, ApJ, 597, 768
Schmitt, H. R., Donley, J. L., Antonucci, R. R. J., Hutchings, J. B., & Kinney, A. L. 2003b, ApJS, 148, 327
Stoklasová, I., Ferruit, P., Emsellem, E., et al. 2009, A&A, 500, 1287
Storchi-Bergmann, T., Lopes, R. D. S., McGregor, P. J., et al. 2010, MNRAS, 402, 819
Unger, S. W., Pedlar, A., Axon, D. J., et al. 1987, MNRAS, 228, 671
Veilleux, S., Cecil, G., & Bland-Hawthorn, J. 2005, ARA&A, 43, 769
Veilleux, S., Meléndez, M., Sturm, E., et al. 2013, ApJ, 776, 27
Villar-Martín, M., Arribas, S., Emonts, B., et al. 2016, MNRAS, 460, 130
Wang, J.-M., Chen, Y.-M., Yan, C.-S., Hu, C., & Bian, W.-H. 2007, ApJL, 661, L143
Woo, J.-H., Bae, H.-J., Son, D., & Karouzos, M. 2016, ApJ, 817, 108
York, D. G., Adelman, J., Anderson, J. E., Jr., et al. 2000, AJ, 120, 1579
Young, A. J., Wilson, A. S., & Shopbell, P. L. 2001, ApJ, 556, 6
Zakamska, N. L., Strauss, M. A., Krolik, J. H., et al. 2003, AJ, 126, 2125